Journal of Solid Mechanics Vol. 17, No. 2 (2025) pp. 118-158
DOI: 10.60664/jsm.2025.1126000

Research Paper

Supersonic Flutter and Vibration Analyses of A Functionally Graded Porous-Nanocomposite Sandwich Microbeam

M.H. Hashempour [1], A. Ghorbanpour Arani [1*], Z. Khoddami Maraghi [2], I. Dadoo [1], S. Amir [1]

[1] *Department of Solid Mechanics, Faculty of Mechanical Engineering, University of Kashan, Kashan, Iran*
[2] *Faculty of Engineering, Mahallat Institute of Higher Education, Mahallat, Iran*

Received 6 July 2024; Received in revised form 23 October 2024; Accepted 1 December 2024

ABSTRACT

The present study investigates free vibration and flutter instability analyses of a sandwich microbeam subjected to supersonic fluid flow. The microbeam comprises functionally graded (FG) porosity cores, with top and bottom sheets reinforced by carbon nanotubes (CNTs). Mechanical properties of FG porous-nanocomposite sandwich microbeam are determined using the rule of mixture and the Ashleby-Mori-Tanaka method. Euler-Bernoulli, Timoshenko, and Reddy beam theories are used while the modified couple stress theory (MCST) accounts for size effects. linearized piston theory and Pasternak foundation is considered to model supersonic fluid flow and elastic medium. In the analysis of free vibrations, natural frequencies and corresponding mode shapes are extracted and in flutter analysis, the variations in natural frequencies with respect to the aerodynamic pressure of the fluid flow are plotted to calculate the critical pressure. A parametric study is conducted to investigate the impact of various characteristics include the geometric properties porosity and distribution pattern of pores, mass fraction, type and distribution pattern of CNTs, length scale parameter, and boundary conditions. Based on the results, it can be concluded that using CNTs with smaller chiral indices leads to a maximum increase in the microbeam's natural frequencies and achieves the highest aeroelastic stability. The findings of this research can be utilized in the design and analysis of microturbines as well as equipment used in biomechanical engineering.

Keywords: Free vibration; Flutter; Supersonic fluid flow; Sandwich microbeam; Composite materials; Porous core.

*Corresponding author. Tel.: +98 31 55912450, Fax: +98 31 55912424.
E-mail address: aghorban@kashanu.ac.ir (A. Ghorbanpour Arani)

1 INTRODUCTION

DUE to the importance of investigating free vibrations and aeroelastic stability analysis of microbeams and nanobeams, many researchers have focused on studying the free vibrations and flutter of these structures. The main difference between the studies conducted lies in the material of the structure and the theory used to model size effects for microbeams and nanobeams. Among the materials used in such structures, considering their properties, are porous materials and CNTs. Porous materials are those with many tiny pores incorporated in them, thereby causing their density to be considerably low. When these materials are used in a structure, they reduce the mass of the structure significantly. However, the density of porous materials is not the only positive attribute; they are also highly recyclable, good sound insulators, highly energy absorbent, and have a low thermal conductivity coefficient at zero. These benefits have further improved the use of porous materials in various engineering fields such as aerospace, automotive, civil, and biomechanics. CNTs exhibit exceptional mechanical properties, including high tensile strength, high elastic modulus, and low density. These properties make CNTs an attractive reinforcement material for composites, offering significant improvements in strength, stiffness, and toughness. Additionally, CNTs possess unique electrical and thermal properties, making them promising candidates for various applications in electronics, energy storage, and sensors. Subbaratnam [1] in a study, developed a precise analytical solution using the Energy Method to predict the dynamic instability bounds of simply supported beams on an elastic foundation, with an emphasis on dynamic stability boundaries. They used a single-term trigonometric function to determine the regions of dynamic instability. For the analysis, they employed the Euler-Bernoulli beam theory (EBT) and found that as the value of the elastic foundation parameter increases, the width of the dynamically unstable zones decreases, making the beam less susceptible to dynamic instability phenomena under periodic loads. Magnucki et al. [2] investigated the dynamic stability of a simply supported three-layer beam subjected to a pulsating axial force. They developed two analytical models of this beam; one model considers the nonlinear hypothesis of cross-section deformation, while the other adheres to the standard "broken line" hypothesis. Based on Hamilton's principle, they determined the equations of motion for each of these models. They calculated the stable and unstable regions for three cases of pulsating loading.

Sourani et al. [3] studied the nonlinear dynamic stability of a viscoelastic piezoelectric nano/microplate reinforced with CNTs under time-dependent harmonic biaxial compressive mechanical loading. They found that incorporating a smart foundation reduces the dynamic instability region by over 60% for a constant magnetic field intensity. The stability responses with the smart foundation also show better convergence. Additionally, the system's stability shifts toward higher excitation frequencies and greater overall stability. Addou et al. [4] investigated the effect of porosity on the static and dynamic behavior of laminated composite shells using a novel high-order shear deformation theory. The proposed model considers five unknown variables with a new sinusoidal shear function that accurately distributes transverse shear stresses through the shell thickness. For this purpose, three different porosity distributions along the thickness are considered in this study. In the first model, the same percentage of micro-holes is present throughout the thickness. In the second model, the porosity percentage is higher at the top and bottom surfaces, and conversely, in the third model, the porosity percentage is highest at the middle axis. In another study, Van et al. [5] investigated the static bending and natural vibration characteristics of FG material (FGM) doubly laminated plates equipped with shear connectors. The fundamental equations were comprehensively described and developed in this research using the finite element method (FEM) in conjunction with the well-known first-order shear deformation theory (FSDT). They also conducted parametric studies to investigate the effect of geometrical and material properties on the structural response of FGM plates, focusing on thickness variation and distribution of shear connectors. They demonstrated that the numerical results obtained from this study can serve as a valuable benchmark for further research efforts in this area. Madhumita Mohanty et al.[6] analyzed the parametric stability of a non-uniform Timoshenko sandwich beam using computational methods, which is situated on a Pasternak foundation with a non-constant spring stiffness parameter. The governing equation of motion and the associated boundary conditions are defined using Hamilton's principle and are non-dimensionalized using the main principle of the Galerkin method. They examined the regions of parametric instability considering the effects of several system parameters and geometric parameters, and presented the results through a series of plots.Civalek et al. [7] investigated the dynamics of functionally graded porous microbeams made of metal foam with deformable boundaries. They used the nonlocal strain gradient elasticity theory to account for scale effects and utilized Stokes' transformation along with Fourier sine series to solve the governing differential equations. Their results showed that porosity distribution, type of material distribution, elastic environment, and rotational stiffness affect the free vibration frequencies of micro beam. Also, the deformation of the boundaries reduces the natural frequencies of the micro beam. Ghorbanpour-Arani et al. [8] investigated the frequency response of a smart sandwich plate composed of magnetic face sheets and a nanofiber-reinforced core. The analysis employed the third-order shear deformation theory (Reddy's theory). It revealed insightful details regarding the influence of various parameters, including in-plane forces, elastic foundation modulus, core-to-face sheet thickness ratio, and velocity feedback gain controller on the dimensionless frequency of the sandwich plate. Due to the significance of investigating free vibrations and analyzing the aeroelastic stability of microbeams and nanobeams, numerous researchers have focused on studying these structures' free vibrations and flutter. The main difference between the conducted studies lies in the structure's material and the theory used to model the size effects for microbeams and nanobeams. Notably, while the number of research studies conducted on the analysis of free vibrations of microbeams and nanobeams is considerable, the number of research studies presented on the aeroelastic stability analysis of microbeams and nanobeams is limited. In a recent study, Gia et al. [9] investigated the size-dependent nonlinear vibration of functionally graded carbon nanotubes reinforced composite (FG-CNTRC) and piezoelectric layers in thermal environments. They accurately analyzed and investigated the influence of the nonlocal parameter, material length scale parameter, geometric properties of the microbeam, temperature change, applied voltage, distribution pattern, and volume fraction of CNTs on the nonlinear free vibration behavior of FG-CNTRC microbeams. The results demonstrated that the nonlocal parameter, material length scale parameter, temperature change, applied voltage, and distribution pattern of CNTs have a significant impact on the nonlinear free vibration frequencies of the FG-CNTRC microbeams. They concluded that the FG-CNTRC microbeams vibrate with lower nonlinear vibration frequencies in a warmer environment. The researchers studied the influence of the pore distribution pattern and porosity coefficient on the natural frequencies of the microbeam. Free vibration analysis of cracked microbeams was investigated by Wu et al. [10]. They employed the Timoshenko beam theory (TBT) and the MCST to model the microbeam. They demonstrated that the presence of a crack in the microbeam leads to a decrease in natural frequencies, depending on its location and depth. Free vibration and flutter analyses for FG nanobeams were investigated by Moatallebi et al. [11]. They incorporated surface effects into their modeling and demonstrated that the significance of surface effects increases as the aspect ratios of width-to-length and thickness-to-length for the nanobeam decrease. Static bending, mechanical buckling, and free vibration analyses of porous microbeams with a two-dimensional distribution of pores across the thickness and length of the microbeam were investigated by Karamanli and Wu [12]. They employed the modified strain gradient theory to model the microbeam and assumed that the length scale parameter varies along the longitudinal direction. They further studied the impact of this variation on the static deflection, critical buckling load, and natural frequencies of the microbeam. Free vibration analysis of a sandwich microbeam with a porous fluid-saturated core and graphene nanoplatelet-reinforced polymer faces was investigated by Arshid and Amir [13]. They studied the influence of various parameters on the microbeam's natural frequencies, including the core's porosity coefficient and the mass fraction of graphene nanoplatelets (GNPs) added to the faces. Vibration analysis of porous FG microbeams was investigated by Tlidgi et al. [14]. A salient feature of this study was the employment of a MCST coupled with a quasi-3D beam theory for modeling the microbeam. The researchers studied the influence of the pore distribution pattern and porosity coefficient on the natural frequencies of the microbeam. Haghparast et al. [15] investigated the influence of fluid-structure interaction (FSI) on the vibration of a moving sandwich plate with a balsa wood core and nanocomposite face sheets. This study presents a theoretical analysis of the vibrations of a vertically moving sandwich plate floating on a fluid. The plate comprises a balsa wood core and two nanocomposite face sheets vibrating as an integrated sandwich. The FSI effect on the stability of the moving plate is considered for both ideal and viscous fluid conditions. The results indicate that the dimensionless frequencies of the moving sandwich plate decrease rapidly with increasing water levels and become almost independent of the fluid level when it exceeds 50% of the plate length. Static bending, mechanical buckling, and free vibration analyses of porous nanobeams were investigated by Enayat et al. [16] They employed the nonlocal strain gradient theory to model the nanobeam. They found that increasing the porosity coefficient leads to an increase in static deflection, a decrease in the critical buckling load, and an increase or decrease in natural frequencies depending on the pore distribution pattern. Vibration and flutter analysis of rotating sandwich nanobeams with a magneto-rheological core and variable cross-section was investigated by Ghorbanpour Arani and Soleimani [17]. They employed the modified strain gradient theory to model the nanobeam and demonstrated that increasing the rotational speed of the nanobeam enhances its aeroelastic stability. Amir et al. [18] investigated the free vibration of sandwich microbeams with a porous core under thermal loading. They based the microbeam modeling on the MCST. They demonstrated that increasing the porosity coefficient and ambient temperature leads to a decrease in the natural frequencies of the microbeam. Wang et al. [19] investigated bending and free vibration analyses of thick porous microbeams. They employed the sinusoidal shear deformation theory to model the beam and incorporated size effects using the modified strain gradient theory. Due to using the exact Navier solution method for the governing equations, their results were only reported for supported microbeams.

This study focuses on the free vibration and flutter (aeroelastic instability) analyses of a sandwich microbeam exposed to supersonic fluid flow, presenting several innovative contributions to the fields of microbeam analysis and aeroelastic stability. The integration of functionally graded (FG) porous cores in the microbeam design represents a novel approach, enabling a customized distribution of material properties to improve both the performance and stability of the structure. Reinforcing the microbeam, particularly with CNTs featuring smaller chiral indices, significantly boosts its natural frequencies and aeroelastic stability. The study's originality lies in its inventive combination of advanced materials, sophisticated modeling techniques, and thorough parametric analysis, providing deeper insights into the behavior and optimization of sandwich microbeams in aeroelastic environments. Moreover, it can be emphasized that the simultaneous analysis of multiple factors within a single problem introduces further innovation. The findings of this research offer valuable contributions to the development of microturbine designs and biomechanical engineering applications.

2 MATHEMATICAL MODELING

In Fig.1, a sandwich microbeam is placed over an elastic foundation and exposed to a supersonic fluid flow with a density of ρ_∞ and at a velocity of U_∞ . A sandwich microbeam is characterized by a length L and a thickness h , containing a porous core with a thickness h_c , whereas the two polymer-based facings reinforced with CNTs with equal thickness $h_b = h_t$.

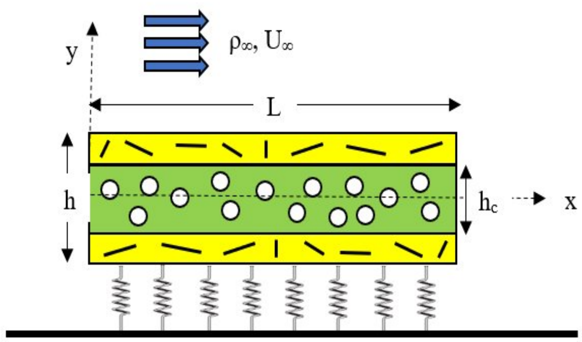

Fig . 1

The geometry of an FG porous-nanocomposite sandwich microbeam.

In the following research, porous materials, core, top and bottom sheets, and CNTs are explained. Then, the method for calculating the mechanical properties of the core, top and bottom sheets is investigated. Finally, using these calculations and applying Hamilton's principle, the system energy is calculated.

3 MATHEMATICAL FORMULATION

3.1 Porous Core Modeling

Based on what was mentioned in the introduction, three types of porosity distributions can be considered: Uniform distribution (U), Symmetric Type I (SI), and Symmetric Type II (SII) (as shown in Fig. 2).The size of pores for the Uniform distribution is constant for the whole core, so the core is homogeneous. For the type SI and type II, the size changes along the thickness of the microbeam core, so the core is inhomogeneous. In this study, a porous material with a porosity distribution of *SI* and of type drain has been used. Drain porous materials are engineered substances designed to facilitate the flow of fluids, such as water or air, through their porous structure. They are commonly used in applications like drainage systems, filtration, and soil stabilization to prevent water buildup and promote proper drainage. These materials typically feature interconnected pores that allow fluid to pass while filtering out solids or other unwanted particles. Their high permeability and durability make them ideal for managing fluid flow in various environmental and industrial contexts.

The variation of the active core in terms of the elastic modulus is defined in [20,21,22].

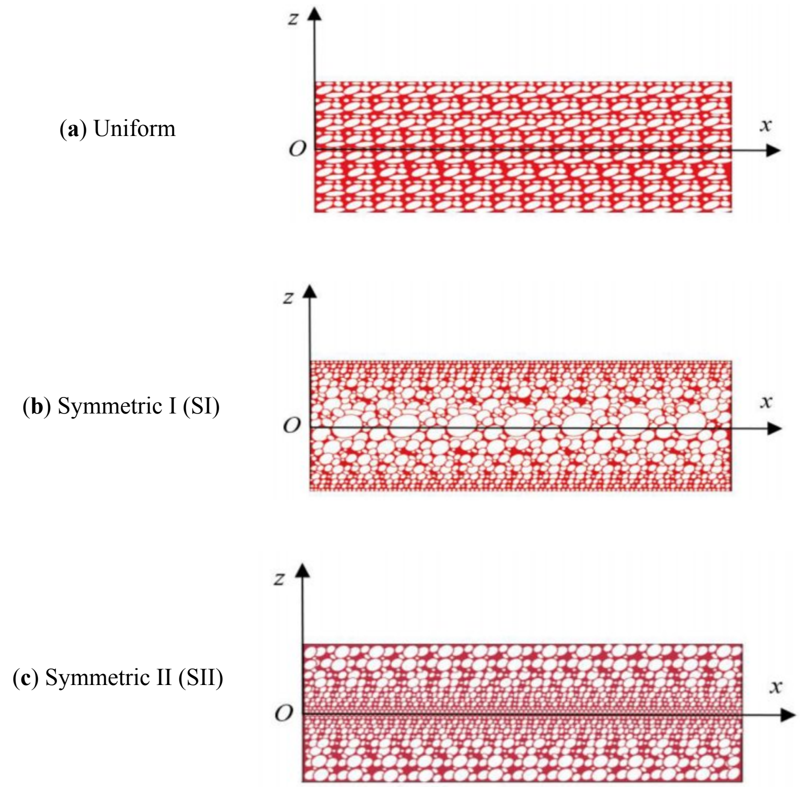

Fig. 2

Holes distribution pattern in the porous core [22].

According to Fig. 2, in the Symmetric Type I distribution pattern, the pores near the mid-surface $(z = 0)$ are larger, and the size of the pores decreases as one moves toward the lower and upper surfaces of the core ($z = \pm 0.5h_c$), such that there are no pores present at the core surfaces. In contrast, the Symmetric Type II distribution pattern exhibits a completely opposite trend, where the pores near the lower and upper surfaces of the core are larger, and the size of the pores decreases as one moves toward the mid-surface, resulting in no pores at the mid-surface.

$$E_c = E_0 f\left(z\right) \tag{1}$$

In Eq.(1), $f\left(z\right)$ is used to denote different distributions. Moreover, in the subsequent expressions, the subscript c is represented for the mechanical properties of the core and the subscript 0 is for the mechanical properties of porous material. The equation is defined as:

$$\begin{aligned} &\text{U:} && f(z) = 1-\eta_0, \\ &\text{SI:} && f(z) = 1-\eta_1 \cos\left(\frac{\pi z}{h_c}\right) \\ &\text{SII:} && f(z) = 1-\eta_2\left[1-\cos\left(\frac{\pi z}{h_c}\right)\right] \end{aligned} \tag{2}$$

Assuming that porosity coefficients are given by from which a positive value means that the size of the pores is increasing. E_0 is the elastic modulus of the core when it is not porous, that is $\eta_0 = \eta_1 = \eta_2 = 0$.

In porous materials, the following dependency between date elastic modulus and density ρ_c holds [22] .

$$\frac{E_c}{E_0} = \left(\frac{\rho_c}{\rho_0}\right)^{2.73} = f(z) \tag{3}$$

This leads to the following equation for the density of the porous core:

$$\rho_c = \rho_0 g(z) \tag{4}$$

Where ρ represents the density of the nucleus in the non-porous state, and the function g(z) is given as follows:

$$g(z) = \left[f(z)\right]^{\frac{1}{2.73}} \tag{5}$$

Eq.(6) contains several values of the porosity coefficient η_1 of porosity coefficient which is given with corresponding values of porosity coefficients η_0 and η_2 that can be seen in [21].

$$\begin{aligned} \eta_0 &= 1.944\eta_1^6 - 3.417\eta_1^5 + 2.278\eta_1^4 - 0.6708\eta_1^3 + 0.122\eta_1^2 + 0.6362\eta_1 \\ \eta_2 &= -0.4269\eta_1^3 - 0.009286\eta_1^2 + 1.732\eta_1 \end{aligned} \tag{6}$$

It should be noted that in the case of porous materials, the Poisson's ratio ( ) is constant [20], and under the condition of isotropic behavior for such materials, its shear modulus can be expressed as $G = \dfrac{E}{2(1+\nu)}$ [23].

3.2 Composite face sheets

A brief explanation of CNTs and their properties and applications has been provided. Symbols A and V represent the heterogeneous distribution of nanotubes within the matrix, which in some cases follows the pattern of these letters. This variation in distribution has a significant impact on the mechanical properties of such materials. Based on what was mentioned in the introduction, three types of CNT distributions in the face sheets can be considered:

the Uniform U distribution and two graded inhomogeneous distributions in the shapes of A and V. In the Uniform distribution case, the volumetric fraction of CNTs is the same at all points and forms a homogeneous structure. A and V graded distributions differ from each other in that the volumetric fraction of CNTs is constant on the entire path between 0 and 2, and linearly increases in both faces. Since the volume fraction of CNTs varies by the distribution pattern of CNTs, it is best expressed as stated below [24,25]:

$$\begin{aligned} &U: \quad V_r^b(z) = V_r \\ &A: \quad V_r^b(z) = 2V_r \frac{h_c \pm 2z}{h_c - h} \\ &V: \quad V_r^b(z) = 2V_r \frac{h \pm 2z}{h - h_c} \end{aligned} \tag{7}$$

which is written in the Eq. (7) as positive for face sheets $(0.5\mathrm{h}_c \le \mathrm{z} \le 0.5)h$ and negative for bottom sheets $(-0.5\mathrm{h} \le \mathrm{z} \le -0.5\mathrm{h}_c)$.

The distribution in the volume fraction along the thickness of facesheets is shown in Fig.3.

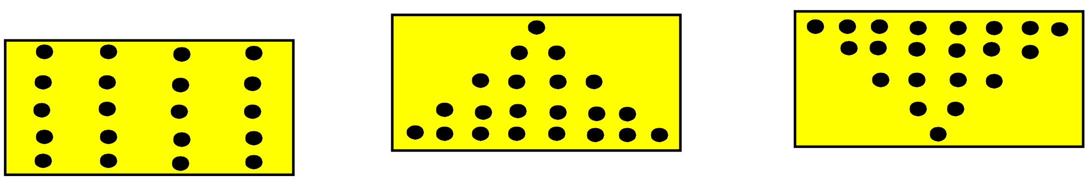

(a) U **(b)** A **(c)** V

Fig . 3

Distribution patterns of CNTs in the face sheets.

In Eq.(7), the variable V_r means the volume fraction of CNTs, which is xpressed as $V_r = \dfrac{1}{1+\dfrac{\rho_r}{\rho_m}\left(\dfrac{1}{w_r}-1\right)}$ [24].

where w_r is the mass fraction , ρ_m is the density of the polymer matrix and ρ_r is the density of the CNTs.Hence, the volume fraction of the polymer matrix in of the microbeam can be derived as:

$$V_m^i = 1 - V_r^i, \quad i = b,t \tag{8}$$

The orientation and aggregation of CNTs do not affect the density of the nanocomposite structure; therefore, the rule of mixtures can be used to calculate it as follows:

$$\rho_i = \rho_m V_m^i + \rho_r V_r^i \quad i = b,t \tag{9}$$

Where b and t indicate the bottom sheet and top sheet, respectively. Additionally, the subscripts m and r indicate the parameters and variables of the mechanical properties of the matrix phase polymer and reinforcement phase CNTs, respectively. Even though the CNTs are anisotropic it is not taken into account for the calculation since they scatter throughout the polymeric matrix isotropically. Since the rule of mixtures cannot accurately calculate the elastic moduli and agglomeration sizes, the Eshelby-Mori-Tanaka method is used. Due to the isotropic structure of the faced overlay coatings, the following equation is used to calculate $\mathrm{E_i}$ and ν_i modulus [26]:

$$E_i = \frac{9K_i G_i}{3K_i + G_i} \quad , \quad \nu_i = \frac{3K_i - 2G_i}{6K_i + 2G_i} \quad i = b,t \tag{10}$$

In Eq. (10), $G_2^* = G_0\left(1 + i\eta_0\right)$ and $G_2^* = G_0\left(1 + i\eta_0\right)$ represent the shear modulus and the bulk modulus of the face sheets respectively, which are calculated as follows [20]:

$$G_i = G_i^{out}\left[1 + \frac{\mu\left(\dfrac{G_i^{in}}{G_i^{out}} - 1\right)}{1 + \left(1 - \mu\right)\left(\dfrac{G_i^{in}}{G_i^{out}} - 1\right)\dfrac{8 - 10\nu_i^{out}}{15\left(1 - \nu_i^{out}\right)}}\right]$$

$$K_i = K_i^{out}\left[1 + \frac{\mu\left(\dfrac{K_i^{in}}{K_i^{out}} - 1\right)}{1 + \left(1 - \mu\right)\left(\dfrac{K_i^{in}}{K_i^{out}} - 1\right)\dfrac{1 + \nu_i^{out}}{3\left(1 - \nu_i^{out}\right)}}\right] \tag{11}$$

The superscripts ‘in’ and ‘out’ relate to the nanotubes inside and outside the agglomeration regions, and the corresponding elastic coefficients are as calculated [30]:

$$K_i^{in} = K_m + \frac{\eta\left(\delta_r - 3K_m\alpha_r\right)V_r^i}{3\left[\mu + \eta\left(\alpha_r - 1\right)V_r^i\right]}, \quad K_i^{out} = K_m + \frac{\left(1-\eta\right)\left(\delta_r - 3K_m\alpha_r\right)V_r^i}{3\left[1 - \mu + \left(1-\eta\right)\left(\alpha_r - 1\right)V_r^i\right]},$$

$$G_i^{in} = G_m + \frac{\eta\left(\eta_r - 2G_m\beta_r\right)V_r^i}{2\left[\mu + \eta\left(\beta_r - 1\right)V_r^i\right]}, \quad G_i^{out} = G_m + \frac{\left(1-\eta\right)\left(\eta_r - 2G_m\beta_r\right)V_r^i}{2\left[1 - \mu + \left(1-\eta\right)\left(\beta_r - 1\right)V_r^i\right]}, \tag{12}$$

$$\nu_i^{out} = \frac{3K_i^{out} - 2G_i^{out}}{6K_i^{out} + 2G_i^{out}}, \quad i = b,t.$$

The subscripts $\mathrm{G_m} = \dfrac{\mathrm{E_m}}{2\left(1 + \upsilon_m\right)}$ and $\mathrm{K_m} = \dfrac{\mathrm{E_m}}{3\left(1 - 2\upsilon_m\right)}$ of and indicate the shear modulus and the bulk modulus of the polymer matrix, which, respectively, are written in terms of the elastic modulus $\mathrm{E_m}$ and Poisson’s ratio υ_m due to the isotropy of the system [26].

In Eqs. (11) and (12), μ and η are dimensionless coefficients known as concentration factors. Additionally, α_r ، β_r ،δ_r ،and η_r are coefficients defined as follows [27]:

$$\alpha_r = \frac{3\left(K_m + G_m\right) + k_r + l_r}{3\left(G_m + k_r\right)}$$

$$\beta_r = \frac{1}{5}\left[\frac{4G_m + 2k_r + l_r}{3(G_m + k_r)} + \frac{4G_m}{G_m + p_r} + 4G_m \frac{3K_m + 4G_m}{G_m(3K_m + G_m) + m_r(3K_m + 7G_m)}\right]$$

$$\eta_r = \frac{1}{5}\left[\frac{2}{3}(n_r - l_r) + \frac{8G_m p_r}{G_m + p_r} + \frac{2(k_r - l_r)(2G_m + l_r)}{3(G_m + k_r)}\right. \tag{13}$$

$$\left. + \frac{8m_r G_m(3K_m + 4G_m)}{3K_m(G_m + m_r) + G_m(G_m + 7m_r)}\right]$$

Hill constants, represented by n_r, m_r, l_r , and k_r, are proportional to the elastic properties of a CNTs as an individual object. The Hill constants can be seen as dependent on the chiral indices of the tube and, therefore, on its shape. Eq. (13) also uuses η and μ for dimensionless coefficients.

η and μ are dimensionless coefficients known as aggregation factors and are represented as $\eta = \frac{W_{agg}}{W_r}$ *and* $\mu = \frac{W_{cluster}}{W}$. where W is the total volume of the nanocomposite structure, W_r is the total volume CNTs, W_{agg} is the volume of the aggregated regions and $W_{eluster}$ is the volume of CNTs inside these regions of aggregation. According to the notion, the more η is closer to 1, the greater the number of nanotubes for which the aggregation effect occurs, and the less μ is, the more densely located are these areas of aggregation. In other words, the closer η is to 1 and μ is to zero, the more aggressive the phenomenon of aggregation, which leads to the greater loss of elastic characteristics of a nanocomposite structure.

The following three scenarios can be considered for these coefficients:

a) $\mu \le \eta \le 1$, which means that some modules of the nanocomposite structure aggregate.
b) Further, (b) $\mu \le \eta = 1$ implies that all modules of the nanocomposite structure are already aggregated.
c) Finally, $\mu = \eta = 1$ states that there is no aggregation at all. Hence, kinetic coefficients dominate over time, as illustrated in Eq.

3.3 Beam theory for sandwich structure

Three theories, namely, EBT, TBT, and Reddy beam theory (RBT), are simultaneously used for microbeam modeling. Then, the displacement field in a general form can be expressed as follows [16]:

$$u_1(x,z,t) = u(x,t) + [c(z) - z]\frac{\partial w(x,t)}{\partial x} - c(z)\psi(x,t)$$

$$u_2(x,z,t) = v(x,t) = 0 \tag{14}$$

$$u_3(x,z,t) = w(x,t)$$

where u_1, u_2 , and u_3 are the displacements in the x, y, and z directions, respectively. In turn, u, v and w determine the corresponding displacements at the mid-surface z=0. After that, ψ determines the rotation about the y-axis and the function $c(z)$ is defined as following [16]:

$$\begin{aligned}&\text{EBT:}\quad c(z)=0\\&\text{TBT:}\quad c(z)=z\\&\text{RBT:}\quad c(z)=z-\frac{4z^3}{3h^2}\end{aligned}\tag{15}$$

Lowers drive modes of a beam constantly include transverse vibrational models, and therefore, only transverse modes participate in the flutter phenomenon, while longitudinal ones do not affect the flutter occurrence. Thus, it is assumed that only transverse vibrations of the beam arise in this study.

The components of all the strain tensors may be written via the strain-displacement relationships as follows [28]:

$$\begin{aligned}&\varepsilon_{xx}=\frac{\partial u_1}{\partial x}\quad,\quad \varepsilon_{yy}=\frac{\partial u_2}{\partial y}\quad,\quad \varepsilon_{zz}=\frac{\partial u_3}{\partial z}\\&\gamma_{yz}=\frac{\partial u_2}{\partial z}+\frac{\partial u_3}{\partial y},\quad \gamma_{xz}=\frac{\partial u_1}{\partial z}+\frac{\partial u_3}{\partial x},\quad \gamma_{xy}=\frac{\partial u_1}{\partial y}+\frac{\partial u_2}{\partial x}\end{aligned}\tag{16}$$

Here, ε_{ij} and γ_{ij} refer to the normal and shear components of the strain tensor, respectively. It can be shown, after substituting Eq.(15) into Eq.(16), that the strain tensor has only two non-zero components:

$$\begin{aligned}&\varepsilon_{yy}=\varepsilon_{zz}=\gamma_{yz}=\gamma_{xy}=0\\&\varepsilon_{xx}=\left[c(z)-z\right]\frac{\partial^2 w}{\partial x^2}-c(z)\frac{\partial\psi}{\partial x}\\&\gamma_{xz}=c'(z)\left(\frac{\partial w}{\partial x}-\psi\right)\end{aligned}\tag{17}$$

3.4 Stress-strain relations

The stress tensor, based on Hooke's law, is expressed as:

$$\gamma_{xz}=c'(z)\left(\frac{\partial w}{\partial x}-\psi\right)\tag{18}$$

Now, with E and G being the elastic and shear moduli, respectively. k_s is introduced as shear correction factor, which in Euler-Bernoulli, Timoshenko, and Reddy beam theories are respectively $k_s=0$, $k_s=\frac{5}{6}$, and $k_s=1$, so the two components of the stress tensor to be expressed:

$$\begin{aligned}&\sigma_{xx}=E_c(z)-z\frac{\partial^2 w}{\partial x^2}-c(z)\frac{\partial\psi}{\partial x}\\&\sigma_{xz}=k_sGc'(z)\frac{\partial w}{\partial x}-\psi\end{aligned}\tag{19}$$

Substituting the function $c(z)$ from Eq.(15) in Eq. (19), and also considering the values of the shear correction factor for the appropriate theories, it is obtained that the components of the stress tensor for three theories:

$$\text{EBT:}\quad \sigma_{xz}=0$$
$$\text{TBT:}\quad \sigma_{xz}=\frac{5}{6}G\left(\frac{\partial w}{\partial x}-\psi\right) \tag{20}$$
$$\text{RBT:}\quad \sigma_{xz}=G\left[1-\left(\frac{2z}{h}\right)^2\right]\left(\frac{\partial w}{\partial x}-\psi\right)$$

3.5 Modified couple stress theory

According to the MCST, in addition to the classical tension tensor, obtained from the force vector passing through each point of the object, a non-classical tension tensor is synthesized from the moment or couple acting on each object point. These components appear as follows [26].

$$m_{ij}=2Gl^2\chi_{ij} \tag{21}$$

Where, l is the length scale parameter and χ_{ij} is curvature tensor, which is calculated using Booth's equation [21]:

$$\chi_{ij}=\frac{1}{4}\left(e_{imn}\frac{\partial^2 u_n}{\partial x_m\partial x_j}+e_{jmn}\frac{\partial^2 u_n}{\partial x_m\partial x_i}\right) \tag{22}$$

where e_{ijk} is the permutation tensor. The non-zero components of the non-classical stress tensor due to couple stress can be written as:

$$m_{xy}=\frac{1}{2}Gl^2\left\{\left[c'(z)-2\right]\frac{\partial^2 w}{\partial x^2}-c'(z)\frac{\partial\psi}{\partial x}\right\} \tag{23}$$
$$m_{yz}=\frac{1}{2}Gl^2c''(z)\left(\frac{\partial w}{\partial x}-\psi\right)$$

In Eq. (23), by replacing $c(z)$ from Eq.(16) in Eq.(23), the non-zero components of the non-classical tensor due to couple stress will be written as:

$$\text{EBT:}\quad m_{xy}=-Gl^2\frac{\partial^2 w}{\partial x^2},\qquad m_{yz}=0,$$
$$\text{TBT:}\quad m_{xy}=-\frac{Gl^2}{2}\left(\frac{\partial^2 w}{\partial x^2}+\frac{\partial\psi}{\partial x}\right),\qquad m_{yz}=0,$$
$$\text{RBT:}\quad m_{xy}=-\frac{Gl^2}{2}\left\{\left[1+\left(\frac{2z}{h}\right)^2\right]\frac{\partial^2 w}{\partial x^2}+\left[1-\left(\frac{2z}{h}\right)^2\right]\frac{\partial\psi}{\partial x}\right\} \tag{24}$$
$$m_{yz}=-4G\left(\frac{l}{h}\right)^2 z\left(\frac{\partial w}{\partial x}-\psi\right)$$

4 GOVERNING EQUATIONS USING THE ENERGY METHOD

Hamilton's principle gives the governing equations for the dynamic behavior of a structure and the corresponding boundary conditions. Hamilton's principle can be obtained:

$$\int_{t_1}^{t_2} \left(\delta T - \delta U - \delta U_f + \delta W_{n.c.} \right) dt = 0 \tag{25}$$

where δ is a variation operator, and $[t_1, t_2]$ is any time interval. T is the kinetic energy of the microbeam, U, is the potential energy of the microbeam, U_f is the potential energy of the substrate, and $W_{n.c,}$ is the work of external forces. The kinetic energy of the microbeam is given by Eq. (14).

$$T = \frac{1}{2} \iiint_V \rho \left[\left(\frac{\partial u_1}{\partial t} \right)^2 + \left(\frac{\partial u_3}{\partial t} \right)^2 \right] dV \tag{26}$$

and variation in kinetic energy is given by:

$$\delta T = b \int_0^L \left(I_5 \frac{\partial^2 w}{\partial t \partial x} \frac{\partial^2 \delta w}{\partial t \partial x} - I_4 \frac{\partial \psi}{\partial t} \frac{\partial^2 \delta w}{\partial t \partial x} - I_4 \frac{\partial^2 w}{\partial t \partial x} \frac{\partial \delta \psi}{\partial t} + I_2 \frac{\partial \psi}{\partial t} + I_0 \frac{\partial w}{\partial t} \frac{\partial \delta w}{\partial t} \right) dx \tag{27}$$

Where l is microbeam rotational inertia, and it is defined in the following expression:

$$\left[I_0, I_1, I_2, I_3 \right] = \int_{-\frac{h}{2}}^{+\frac{h}{2}} \rho(z) \left[1, z^2, c^2(z), zc(z) \right] dz \tag{28}$$

$$I_4 = I_2 - I_3 \qquad , \qquad I_5 = I_2 - 2I_3 + I_1$$

Using MCST, the potential energy of a microbeam can be expressed as:

$$U = \frac{1}{2} \iiint_V \left(\sigma_{ij} \varepsilon_{ij} + m_{ij} \chi_{ij} \right) dV \tag{29}$$

and, in accordance with the previously given Eqs, (18) and (24), it can be rewritten as:

$$U = \frac{1}{2} \iiint_V \left(\sigma_{xx} \varepsilon_{xx} + \sigma_{xz} \gamma_{xz} + 2m_{xy} \chi_{xy} + 2m_{yz} \chi_{yz} \right) dV \tag{30}$$

4.1 External Work

4.1.1 Elastic Medium

According to Pasternak foundation, the substrate potential energy is given by [29,30]:

$$U_f = \frac{b}{2}\int_0^L \left[k_w w^2 + k_p \left(\frac{\partial w}{\partial x} \right)^2 \right] dx \tag{31}$$

Where k_w and k_p are respectively referred to as the Winkler foundation coefficient and the Pasternak foundation coefficient.

The external force q the total upper surface of the microbeam is given by the work $W_{n.c.} = b\int_0^L qwdx$ and the strain of this work can be expressed as $\delta W_{n.c.} = b\int_0^L q\,\delta w dx$.

4.1.2 Aerodynamic pressure

Aerodynamic pressure refers to the pressure generated by the movement of an object through a fluid (typically air). This pressure arises from the interaction between the fluid flow and the surface of the object and is directly related to the flow velocity and the density of the fluid. Aerodynamic pressure plays a critical role in the design and analysis of various structures, including aircraft, automobiles, and buildings, as it can significantly influence phenomena such as lift and drag. Furthermore, a proper understanding of aerodynamic pressure is essential in engineering applications to enhance the performance and safety of structures. Aerodynamic pressure is approximated using linearized piston theory when supersonic fluid flows with Mach number (M_∞) in the range of $\sqrt{2} \le M_\infty \le 5$, [20, 31]:

$$q(x, y, t) = -p_\infty \frac{\partial w}{\partial x} - \mu_\infty \frac{\partial w}{\partial t} \tag{32}$$

In this relation, P_∞ and μ_∞ are known as the aerodynamic pressure and aerodynamic damping, respectively, which are derived by the following equation:

$$\mu_\infty = \frac{M_\infty \left(M_\infty^2 - 2 \right)}{\sqrt{\left(M_\infty^2 - 1 \right)^3}} \rho_\infty U_s \quad , \quad p_\infty = \frac{M_\infty^2}{\sqrt{M_\infty^2 - 1}} \rho_\infty U_s^2 \tag{33}$$

Then, by substituting Eq.(28) into Eq.(26), the governing equation is obtained:

δw :

$$-\frac{\partial Q_{xz}}{\partial x} - \frac{\partial^2 M_{xx}}{\partial x^2} + \frac{\partial^2 P_{xx}}{\partial x^2} - 2\frac{\partial^2 s_{xy}}{\partial x^2} + \frac{\partial^2 r_{xy}}{\partial x^2} - \frac{\partial t_{yz}}{\partial x}$$

$$-bI_5 \frac{\partial^4 w}{\partial t^2 \partial x^2} + bI_0 \frac{\partial^2 w}{\partial t^2} + bI_4 \frac{\partial^3 \psi}{\partial t^2 \partial x} + bk_w w - bk_p \frac{\partial^2 w}{\partial x^2} - bq = 0 \tag{34}$$

$\delta\psi$:

$$Q_{xz} - \frac{\partial P_{xx}}{\partial x} - \frac{\partial r_{xy}}{\partial x} + t_{yz} + bI_4 \frac{\partial^3 w}{\partial t^2 \partial x} - bI_2 \frac{\partial^2 \psi}{\partial t^2}$$

(35)

$$\left(\frac{\partial M_{xx}}{\partial x} + 2\frac{\partial s_{xy}}{\partial x} + bk_p \frac{\partial w}{\partial x} + bI_5 \frac{\partial^3 w}{\partial t^2 \partial x} \right) =$$

In which

$$P_{xx} = \iint c\left(z\right)dA \quad ,M_{xx} = \iint \sigma_{xx}\, z\, dA \quad ,Q_{xz} = \iint \sigma_{xz}\, c\left(z\right)dA$$

(36)

$$S_{xy} = \frac{1}{2}\iint m_{xy}\, dA \quad ,r_{xy} = \frac{1}{2}\iint c\left(z\right)dA \quad ,t_{xy} = \iint m_{yz}\ddot{c}\left(z\right)dA$$

where $t_{xy}, r_{xy}, S_{xy}, Q_{xz}, M_{xx}$ *and* P_{xx} are the resultant forces and moments. In flutter analysis, the aerodynamic damping term does not significantly affect flutter boundaries and increases the computational effort to solve an eigenvalue problem due to the non-standard creation. Therefore, in papers associated with supersonic flutter analysis, the term aerodynamic damping is often neglected $\mu \approx 0$ [32, 33]:

5 SOLUTION PROCEDURE

Dimensonless motion equations can be written by defining time variable $\tau = \frac{t}{L}\sqrt{\frac{E_m}{\rho_m}}$ and space variable $\zeta = \frac{x}{L}$, in a dimensionaless from using separation of variable in the from of Eq.(37):

$$\begin{Bmatrix} w\left(\zeta,\tau\right) \\ \psi\left(\zeta,\tau\right) \end{Bmatrix} = \begin{Bmatrix} LW\left(\zeta\right) \\ \Psi\left(\zeta\right) \end{Bmatrix} exp\left(\lambda\tau\right) \tag{37}$$

λ is a dimensionless eigen value.
Based on the above discussion, the dimensionless boundary conditions can be expressed as follows:

$$W = 0, \quad \frac{dW}{d\zeta} = 0, \quad \Psi = 0 \qquad \text{for clamped boundary condition}$$

(38)

$$W = 0, \quad \frac{d^2W}{d\zeta^2} = 0, \quad \frac{d\Psi}{d\zeta} = 0 \qquad \text{for simple boundary condition}$$

4.1 Differential quadrature method (DQM)

The DQM was first introduced in the early 1970s by Bellman and Casti [34], and Bellman and his colleagues [35]. Since then, it has been used by many researchers, especially for solving problems in mechanical engineering. In this method, the solution interval of the problem is first discretized into a set of grid points. Then, the derivatives of each function in the governing differential equations at each of these points are estimated based on the values of that function at all points in the solution interval. The result of this estimation is the formulation of the governing

equations and boundary conditions as algebraic equations, which are then solved to compute the values of the unknown functions.
Let $f(x)$ be a continuous and differentiable function of $0 \le x \le L$. Once blocked into a mesh with N points, the values of the function at these dots will be a column vector as shown below:

$$\{f\}_{N\times 1} = \begin{Bmatrix} f_1 \\ f_2 \\ \vdots \\ f_N \end{Bmatrix} = \begin{Bmatrix} f(x_1) \\ f(x_2) \\ \vdots \\ f(x_N) \end{Bmatrix} \tag{39}$$

The ▯ derivative values at this discrete distribution points:

$$\begin{Bmatrix} \dfrac{d^n f}{dx^n} \end{Bmatrix} = \left[A^{(n)}\right]\{f\} \tag{40}$$

In Eq.(37), the matrix of coefficient weights associated to the ▯ derivative is given by $[A^{((n))}]$.. That for the first derivative is [33,34]:

$$A_{ij}^{(1)} = \begin{cases} \displaystyle\sum_{\substack{m=1 \\ m\ne i}}^{N} \frac{1}{x_i - x_m}, & i = j, \\ \dfrac{\prod_{\substack{m=1 \\ m\ne i,j}}^{N} (x_i - x_m)}{\prod_{\substack{m=1 \\ m\ne j}}^{N} (x_j - x_m)}, & i \ne j, \end{cases} \qquad i, j = 1, 2, ..., N \tag{41}$$

While that for higher derivatives using [36.37]:

$$\left[A^{(n)}\right] = \left[A^{(1)}\right]\left[A^{(n-1)}\right], \quad n = 2, 3, \ldots, N-1 \tag{42}$$

As for the function itself, i.e., the zero-th derivative, its value can be given as:

$$\{f\} = [I]_{N\times N}\{f\} \tag{43}$$

The optimal pattern is given by quittance to the interval $0 \le x \le L$ is the Chebyshev-Gauss-Lobatto pattern which is produced by Ehrenfrest's method is expressed as [33,34]:

$$x_i = \frac{L}{2}\left[1 - \cos\left(\frac{i-1}{N-1}\pi\right)\right], \quad i = 1, 2, 3, ..., N \tag{44}$$

By employing Eqs.(40) and (43) to write down governing equations, one can have:

$$[K]\{s\} = \lambda^2 [M]\{s\} \tag{45}$$

Where $[K]$ and $[M]$ and $\{S\}$ are the stiffness and mass matrices and the total displacement vector. By nulling out the governing equations at the boundary points, results in the:

$$\left[\tilde{K}\right]\{s\} = \lambda^2 \left[\tilde{M}\right]\{s\} \tag{46}$$

The obtained eigenvectors from the eigenvalue problem solve are the mode shapes of the microbeam vibrations and let complex eigenvectors be obtained as $\lambda = \lambda_R + i\,\lambda_I$, where the real part and the imaginary correspond to λ_R . By using Eqs.(39) and (45):

$$\exp(\lambda\tau) = \exp(\lambda_R \tau + i\,\lambda_I \tau) = \exp(\lambda_R \tau)\left[\cos(\lambda_I \tau) + i\,\sin(\lambda_I \tau)\right] \tag{47}$$

The λ_I essentially represent the dimensionless natural frequency of the microbeam and λ_R indicates the stability or instability of the microbeam vibrations while the fluid flows along its path.

4.2 Navier solution

By Navier method, an accurate solution for the analysis of the free vibration of a microbeam with simple support conditions and removing the fluid flow is provided. The results obtained from this exact solution are used to validate the numerical solution presented using the DQM.

$$W(\zeta) = \sum_{m=1}^{\infty} W_m \sin(m\pi\zeta)$$

$$\Psi(\zeta) = \sum_{m=1}^{\infty} \Psi_m \cos(m\pi\zeta) \tag{48}$$

That is, which generates different vibrational modes as $m = 1,2,3,\ldots$. For free vibration that occurs without fluid flow and damping, then the eigenvalues shall be purely imaginary, expressed as $(\lambda = i\lambda_I)$, and the magnitude of the imaginary part indicates the natural frequencies. Hence, it is expressed as. From the solution of the eigenvalue of Eq. (48), it is determined the natural frequencies of a microbeam with simple support conditions.

$$\left[K\right]_{2\times 2}\begin{Bmatrix} W_m \\ \Psi_m \end{Bmatrix} = \lambda_I^{\,2}\left[m\right]_{2\times 2}\begin{Bmatrix} W_m \\ \Psi_m \end{Bmatrix} \tag{49}$$

6 NUMERICAL RESULTS AND DISCUSSION

6.1 Verification

Table 1 shows a comparison of the first four vibrational modes' natural frequencies using simple supports microbeam. Theory exact value according to Navier of natural frequencies and its approximation with respect of 4 decimals compared with the natural frequencies value. It is evident that these approximate natural frequency values of the Navier method are no difference from the real natural frequency values of the microstructure. However, after decimal 4, it has been shown that simple supports microbeam differences from the exact value. Further investigation represented more decimal places, and this table does not visible these minor differences in subsequent decimal digits.

Table 1
Comparison of the results for different theories

		λ_1	λ_2	λ_3	λ_4
EBT	DQM	1.4685	2.6234	4.3518	6.6041
	Navier	1.4685	2.6234	4.3518	6.6041
TBT	DQM	1.4675	2.5886	4.1527	6.0167
	Navier	1.4675	2.5886	4.1527	6.0167
RBT	DQM	1.4675	2.5858	4.1384	5.9806
	Navier	1.4675	2.5858	4.1384	5.9806

One-layer porous beam: Poisson's ratio $\nu = 1/3$, porosity coefficient $e_1 = 0.5$, distribution pattern SI, no substrate, $k_w^* = k_p^* = 0$. The free vibration analysis in the absence of fluid flow assumes the beam based on the TBT. The dimensionless form of the natural frequency is as follows:

$$\Omega = \omega L \sqrt{\frac{\rho_0 \left(1-\upsilon^2\right)}{E_0}} \tag{50}$$

Non-dimensional natural frequencies of the first vibration mode of microbeams are presented in Table 2 for various boundary conditions and different thickness-to-length ratios. The corresponding values reported by Chen et al. [38] based on the Ritz method and ANSYS software are also presented in this table. A comparison between the results obtained in this study and those reported by Chen et al. [38] demonstrates the accuracy of the analysis. In the flutter analysis, the effect of aerodynamic pressure on natural frequencies and damping coefficients of microbeams is investigated for the first ten vibration modes to identify and show the modes that play a role in the flutter phenomenon. The results show that for the microbeam with the selected characteristics, the first two vibration modes are involved in flutter. Therefore, in the following, the flutter analysis only presents the diagrams of the changes in the imaginary part of the eigenvalues (natural frequencies) and the corresponding real part only for the first two vibration modes as a function of changes in aerodynamic pressure. With the help of these diagrams, which represent the boundaries of aeroelastic stability (flutter boundaries), the critical aerodynamic pressure that leads to a positive real part (negative damping coefficient) in one of the vibration modes is determined.

Table 2
Dimensionless natural frequencies (Ω) of a porous single-layered beam in its first vibrational mode

			CC	CS	SS	CF
h/L=0.02	Peresent	DQM	0.1331	0.0919	0.0589	0.0210
	chen et al.[39]	RITZ	0.1291	0.0891	0.0571	0.0204
	chen et al.[39]	AVSYS	0.1289	0.0891	0.0571	0.0204
h/L=0.05	Peresent	DQM	0.3270	0.2273	0.1466	0.0524
	chen et al.[39]	RITZ	0.3166	0.2203	0.1419	0.0508
	chen et al.[39]	AVSYS	0.3176	0.2201	0.1419	0.0508
h/L=0.1	Peresent	DQM	0.6175	0.4392	0.2887	0.1040
	chen et al.[39]	RITZ	0.5944	0.4242	0.2798	0.1008
	chen et al.[39]	AVSYS	0.6101	0.4227	0.2778	0.1007

6.2 Results

The presented results are for a microbeam clamped -simple (CS): clamped at *x*=0 and simple at *x*=*L* with length scale parameter $\kappa = 0.01$ and the geometric specifications $h/L = 0.1$ and $h_c/h = 0.5$ on a substrate of characteristics $k_w^* = 0.1$ and. The porous core consists of an epoxy polymer with a type SI porosity pattern, and the face sheets are reinforced with single-walled carbon nanotubes $(SWCNT)$ (10,10 , adhering to the A and V patterns for the upper and lower face sheets, respectively. All specifications are detailed in Table 3. It is important to note that all results are presented in dimensionless forms.

Table 3
Properties of the materials in the microbeam under study

Item	E_m	υ_m	ρ_m	η_1	w_r	β
The porous core	2.1	0.34	1150	0.25	-	-
$SWCN$	-	-	-	-	0.01	0.25

In Table 3, η_1 represents the porosity factor, w_r indicates the mass fraction, and β correspond to the agglomeration coefficients for the CNTs.

It is also important to mention that the flutter analysis focuses on a diagram of changes in the natural frequencies, (imaginary part of the eigenvalues denoted by λ_I), and the corresponding eigenvalues' real part termed (λ_R) as a function of changes in the aerodynamic pressure of the fluid flow, p^*.

Table 4 demonstrates the natural frequencies of the microbeam in the first four vibrational modes using the three theories of Euler-Bernoulli, Timoshenko, and Reddy at various points for a number of points in the solution using the DQM. As can be seen, the obtained numerical solution has a very good convergence speed, and reliable results can be obtained using *N*=23 for the first four vibrational modes' natural frequencies. From Table 4, one can see that the microbeam's natural frequency value in each vibrational mode using the Euler-Bernoulli is greater than the corresponding values for the Timoshenko and Reddy theories. The reason for this could be attributed to the fact that the Euler-Bernoulli theory neglects the effects of shear tractions, which makes the microbeam's stiffness to be underestimated. Thus, the obtained values are higher but inaccurate.

For the case of simple supports at both ends of the microbeam, the natural frequencies of the first four vibration modes were compared for different theories with the corresponding exact values obtained using the Navier solution method. As can be seen, with an approximation of the results up to four decimal places, there is no difference between the approximate values obtained from the DQM and the exact values obtained from the Navier method. Investigations show that slight differences are observed in the subsequent decimal places, which are not visible in this table.

Table 4
Convergence the results in DQM

Theory	Mode	N=11	N=13	N=15	N=17	N=19	N=21	N=23	N=25
EBT	1	1.5673	1.5674	1.5674	1.5674	1.5674	1.5674	1.5674	1.5674
	2	2.8887	2.8890	2.8889	2.8889	2.8889	2.8889	2.8889	2.8889
	3	4.7727	4.7865	4.7859	4.7859	4.7859	4.7859	4.7859	4.7859
	4	7.6559	7.1440	7.1994	7.1939	7.1943	7.1943	7.1943	7.1943
TBT	1	1.5549	1.5524	1.5512	1.5505	1.5500	1.5498	1.5496	1.5495
	2	2.7948	2.7862	2.7813	2.7783	2.7765	2.7753	2.7745	2.7739
	3	4.4394	4.4197	4.4088	4.4024	4.3984	4.3958	4.3941	4.3930
	4	6.3992	6.3181	6.3018	6.2897	6.2821	6.2771	6.2738	6.2716
RBT	1	1.5530	1.5509	1.5498	1.5493	1.5490	1.5488	1.5488	1.5487
	2	2.7879	2.7792	2.7743	2.7715	2.7700	2.7691	2.7686	2.7683
	3	4.4107	4.3945	4.3850	4.3799	4.3771	4.3757	4.3749	4.3746
	4	6.3615	6.2705	6.2566	6.2459	6.2398	6.2364	6.2345	6.2336

Natural frequencies of microbeams for various boundary conditions are reported in Table 5, and the corresponding vibration mode shapes are shown in Fig. 4. As can be seen, for all vibration modes, the highest natural frequencies always belong to the double-clamped microbeam. This is due to the maximum rigidity of the boundaries in this type of boundary condition. The table also shows that the lowest natural frequencies belong to the cantilever microbeam, which is due to the free end of the microbeam and the absence of any constraint at this boundary.

Table 5
Influence of boundary conditions on the natural frequencies of the sandwich microbeam

	λ_1	λ_2	λ_3	λ_4
CC	1.6474	2.9638	4.6150	6.4859
CS	1.5488	2.7686	4.3749	6.2345
SS	1.4675	2.5858	4.1384	5.9806
CF	1.1597	2.0636	3.4020	5.0804

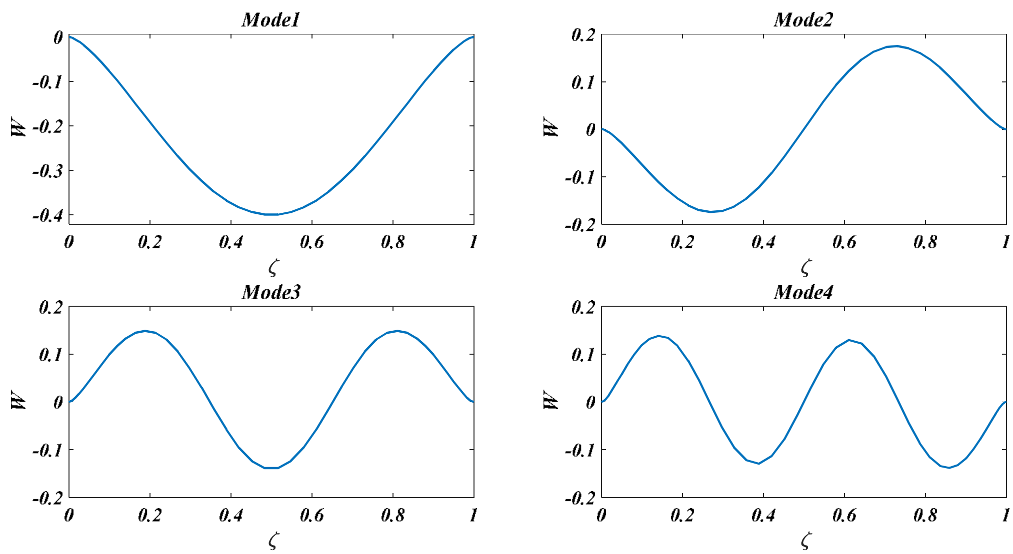

a.C-C boundary conditions

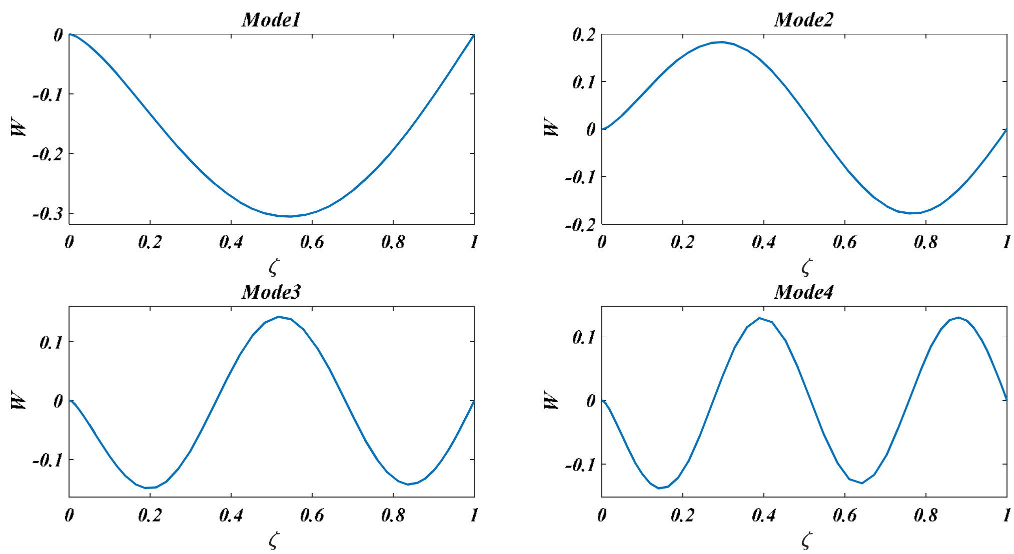

b. C-S boundary conditions

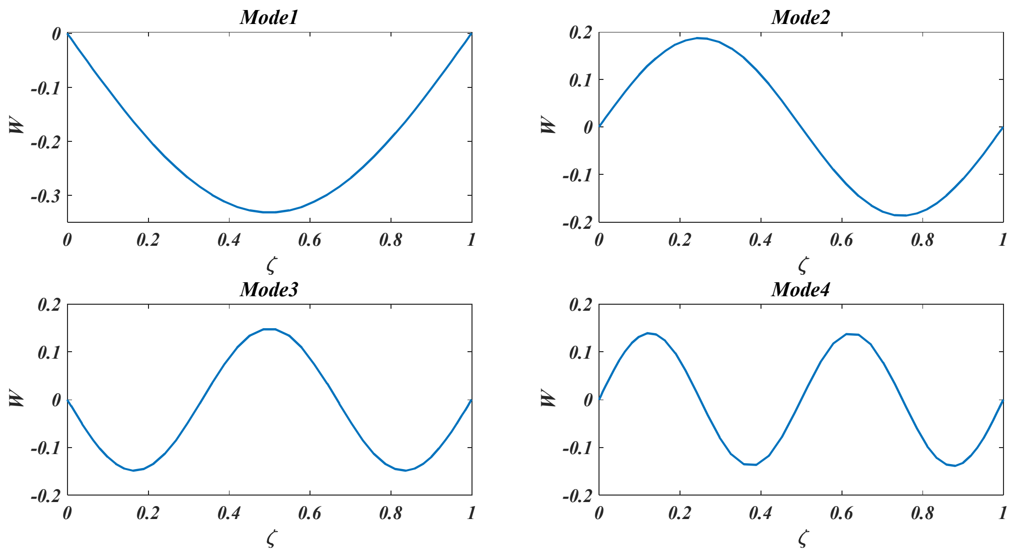

c.S-S boundary conditions

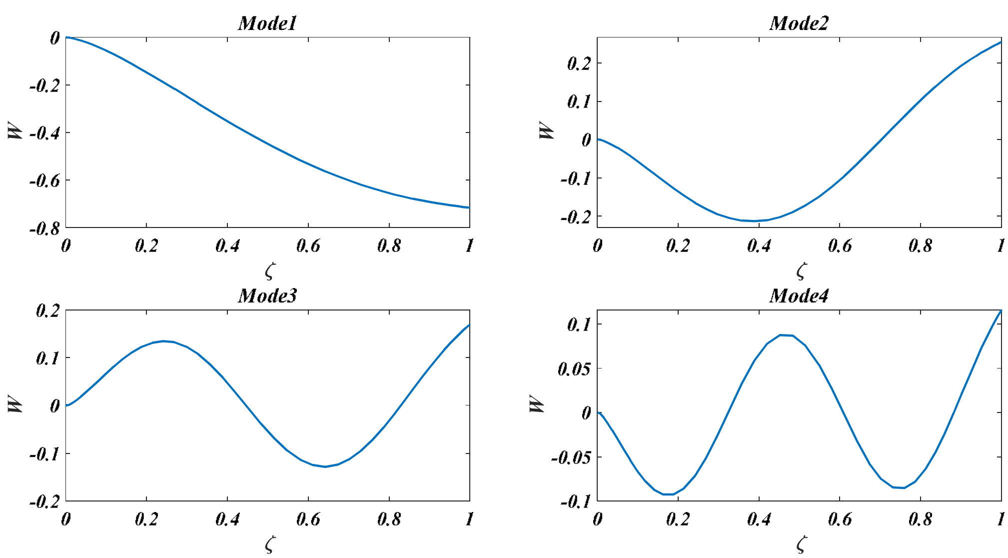

d.C-F boundary condition

Fig. 4
Mode shapes of the sandwich microbeam under various boundary conditions.

7 INSTABILITY ANALYSIS

In this section, the influence of boundary conditions has been considered without applying any additional pressure. As illustrated, when Aerodynamic pressure (increase in fluid velocity) increases and, more accurately, at one specific point, the bodies of the real parts of the eigenvalues split in a way that the real part of one of them turns positive. Hence, the damping coefficient of the corresponding mode turns negative and, therefore, dynamic instability of linear type occurs in the microbeam, which, here, is flutter [36].

The influence of boundary conditions on the aeroelastic stability boundaries of microbeams is investigated in Fig.5. As observed, with an increase in aerodynamic pressure (increase in fluid velocity) beyond a critical value, the real parts of the eigenvalues experience a bifurcation, coinciding with the superposition of the first and second vibrational modes, marking the onset of flutter. Specifically, critical aeroscope forces of the microbeam with CC boundary conditions are the highest, and those of the microbeam with just one clamped end are the lowest; in other words, the microbeam with the smallest number of degrees of freedom at its boundaries has the most restricted motion in the lateral direction. At the same time, the difference between these values is as significant as 37%.

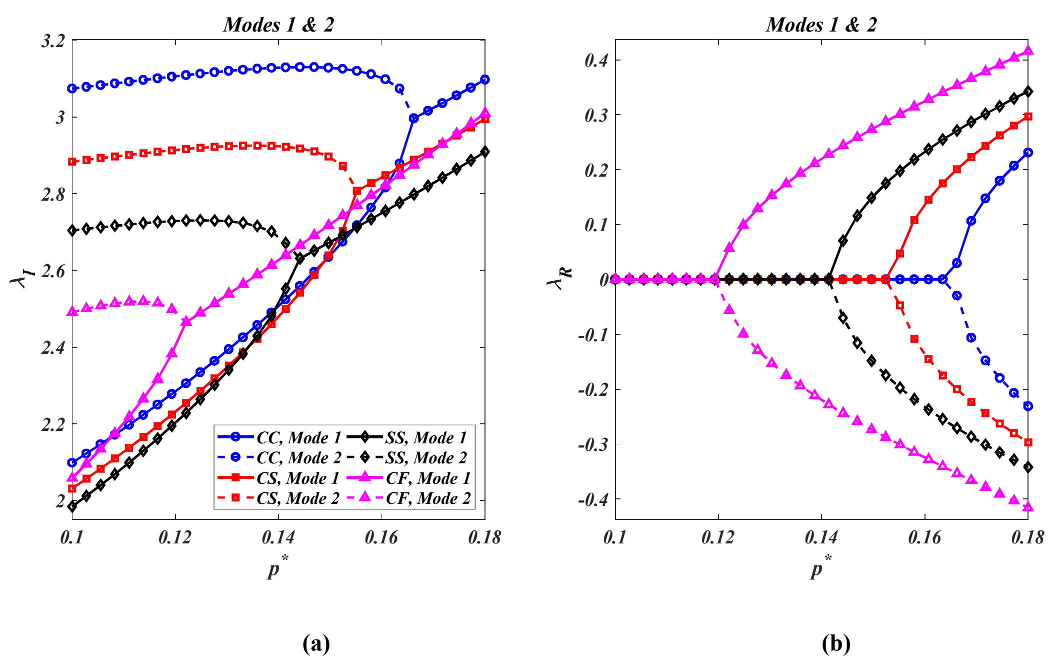

Fig. 5

Influence of boundary conditions on the aeroelastic stability of the sandwich microbeam. (a) The imaginary part of frequency and (b) The real part of frequency.

Figure 5.b refers to the imaginary part of the frequency, where a decrease or increase can be observed. The imaginary part of a frequency, often referred to in the context of complex eigenvalues, is associated with damping in dynamic systems. When analyzing the stability of a system, the frequency can be expressed as a complex number, where the real part represents the oscillation frequency, and the imaginary part indicates the damping behavior.

Specifically, a negative imaginary part suggests that the system experiences damping, leading to a decrease in amplitude over time. Conversely, a positive imaginary part indicates instability, where oscillations may grow without bound. Thus, the imaginary component is crucial for understanding how quickly a system returns to equilibrium after being disturbed, with its magnitude directly related to the rate of energy dissipation or the speed of damping.

In Figs. 7, 9, 11, 13, 14, 16, 17, 20, 22, and 24 alongside the curves taken from the real part of the vibration frequency, the image part is also depicted.

The impact of the length scale parameter on the natural frequencies and aeroelastic stability of the microbeam is illustrated in Fig.6 and Fig. 7, respectively. As the length scale parameter increases, the natural frequencies of the microbeam increase, revealing an enhanced aeroelastic stability. As indicated in Fig. 7, as the dimensionless length scale parameter rises from $\kappa = 0$ to $\kappa = 0.03$, the critical aerodynamic pressure increases by nearly 9 percent.

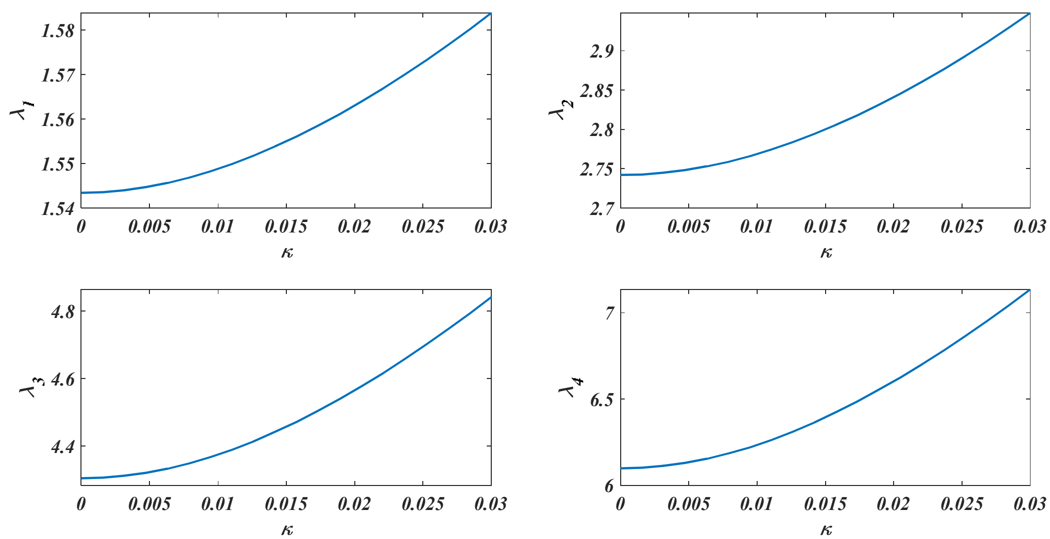

Fig .6

Influence of the length scale parameter on the natural frequencies of the sandwich microbeam.

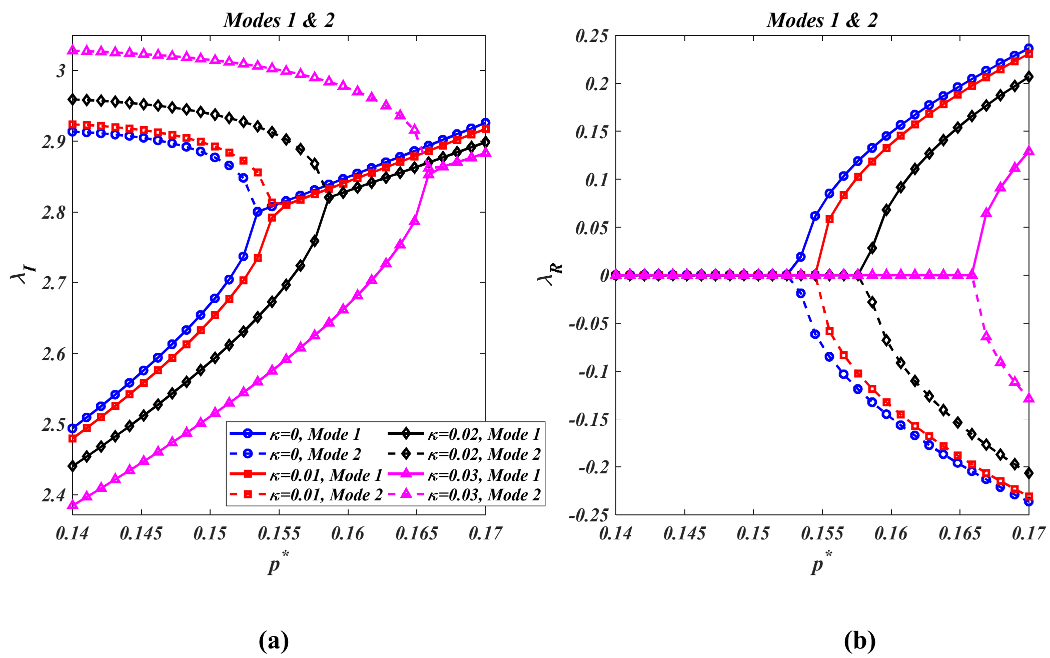

Fig. 7

Influence of the length scale parameter on the aeroelastic stability of the sandwich microbeam. (a) The imaginary part of frequency and (b) The real part of frequency.

Fig. 8 and Fig. 9 focus on analyzing the effects of the thickness-to-length ratio on the natural frequencies and aeroelastic stability boundaries of the microbeam. At any given length of the microbeam, increasing its thickness leads to a significant increase in its stiffness, improving its aeroelastic stability boundaries as evidenced by Fig. 9. Following that figure the critical aerodynamical pressure increases by approximately 17% from $h/L = 0.11$ to $h/L = 0.08$. Increasing the thickness of the microbeam also results in an increase in the mass of the microbeam associated with its increased stiffness, as observed in Fig. 8.

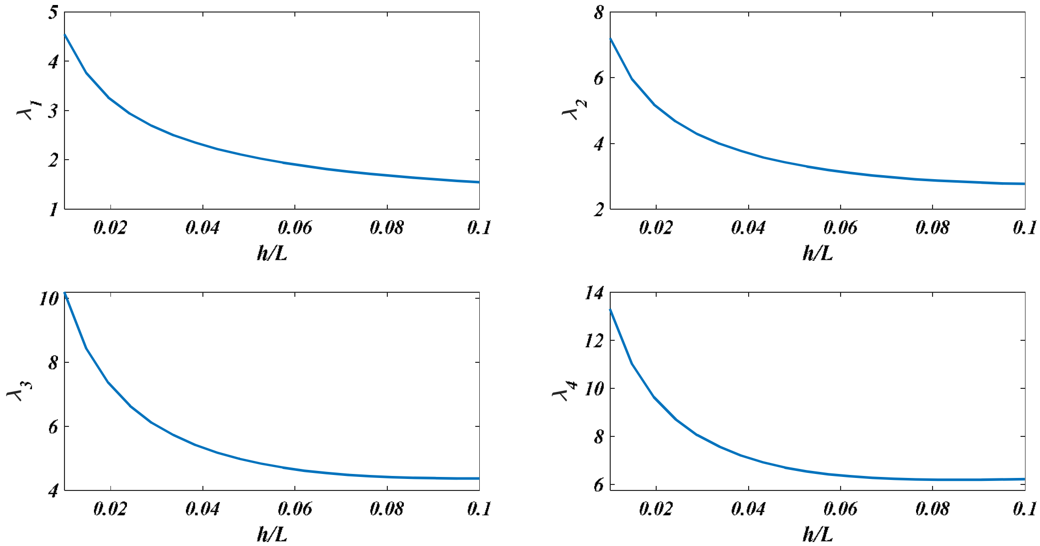

Fig. 8

Influence of the thickness-to-length ratio on the natural frequencies of the sandwich microbeam.

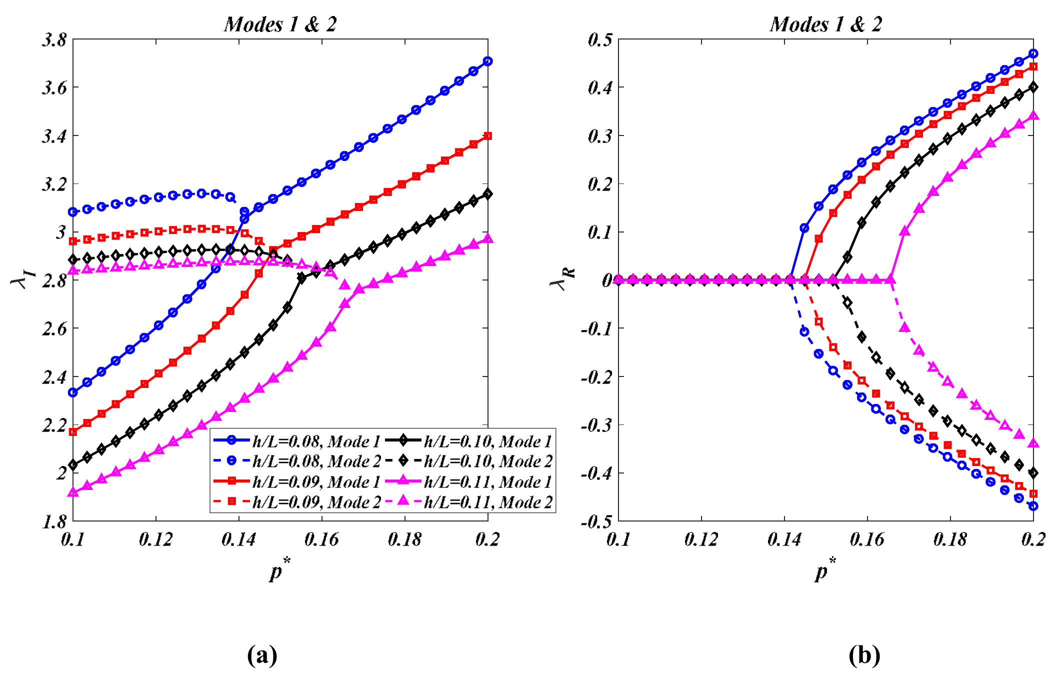

Fig.9

Influence of the thickness-to-length ratio on the aeroelastic stability of the sandwich microbeam. (a) The imaginary part of frequency and (b) The real part of frequency.

By specifying a certain value for the total thickness of a microbeam, the influences of the core thickness ratio to the total thickness upon the natural frequencies and aeroelastic stability boundaries of the microbeam are presented in Figs.10 and Fig.11. Pores in the core make it less stiff or more flexible compared with nanocomposite facings reinforced with CNTs and at the same time mass is less due to the lower density. Therefore, by having a certain value for the total thickness of a microbeam, by increasing the thickness of the porous core, the stiffness and mass of the microbeam reduce simultaneously. Reduction in stiffness decreases the aeroelastic stability, which is seen in Fig. 11. This figure illustrates that increasing the core thickness ratio to the total thickness from $h_c / h = 0.75$ to $h_c / h = 0$ to, critical aerodynamic pressure reduced by about 6 %.

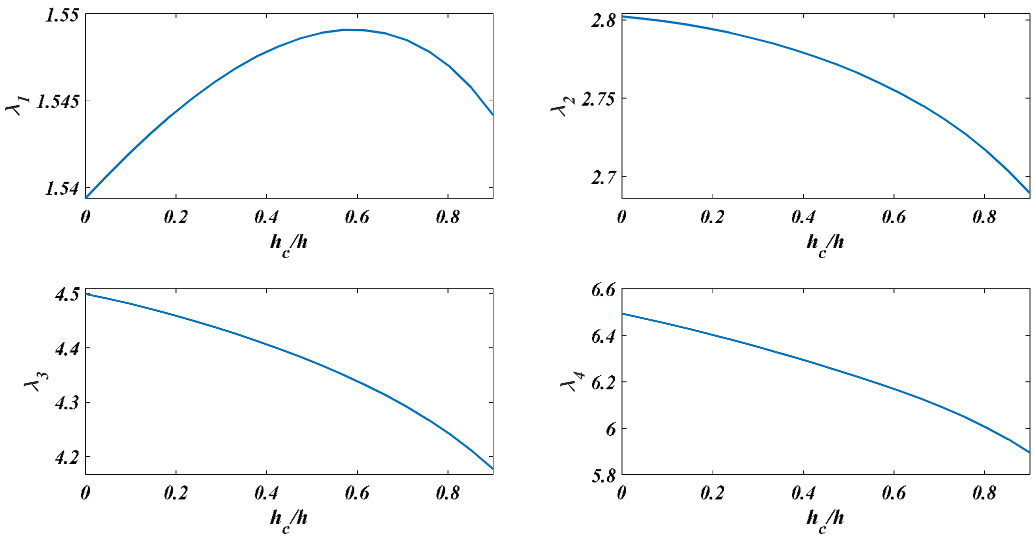

Fig.10

Influence of the core thickness ratio to the total thickness on the natural frequencies of the sandwich microbeam.

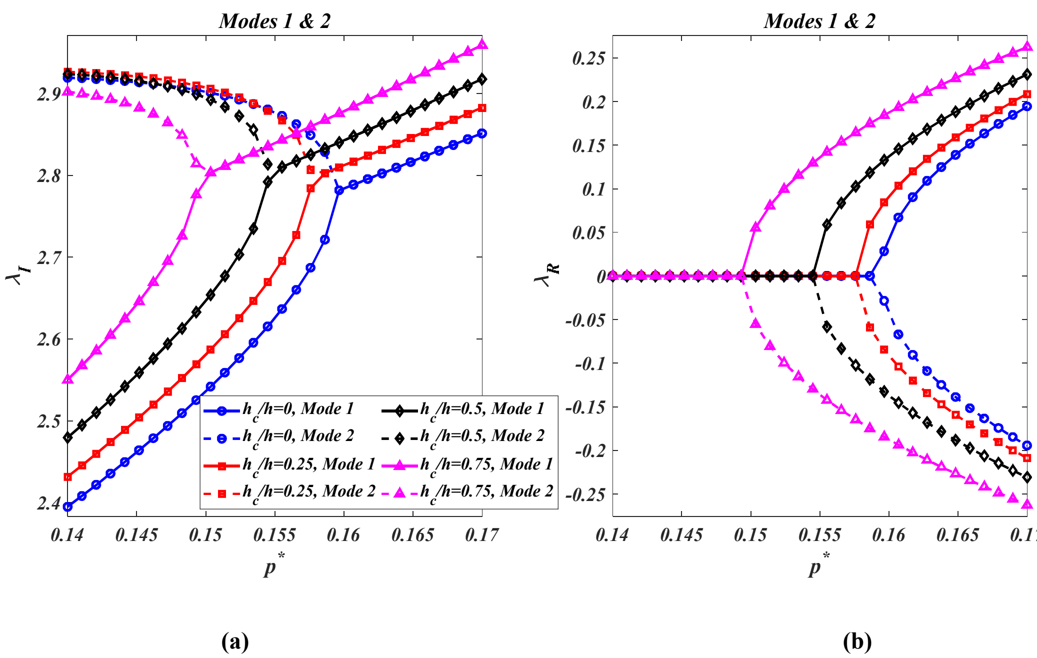

Fig . 11

Influence of the core thickness ratio to the total thickness on the aeroelastic stability of the sandwich microbeam. (a) The imaginary part of frequency and (b) The real part of frequency.

Fig.12 and Fig.13 investigate the effects of the porosity coefficient on the natural frequencies and aeroelastic stability boundaries of microbeams. Increasing the porosity coefficient implies a reduction in the microbeam's stiffness, which, as shown in Fig.13, leads to a decrease in the aeroelastic stability of the microbeam. According to Fig.13, the reduction in critical aerodynamic pressure of the microbeam is negligible for a significant increase in porosity coefficient, such that with an increase in porosity coefficient from 0 to 0.5, the critical aerodynamic pressure decreases by less than one percent. The reason for the small magnitude of this effect is that a very small percentage of the microbeam's stiffness is attributed to its porous core, and a higher percentage is attributed to the nanocomposite skins.

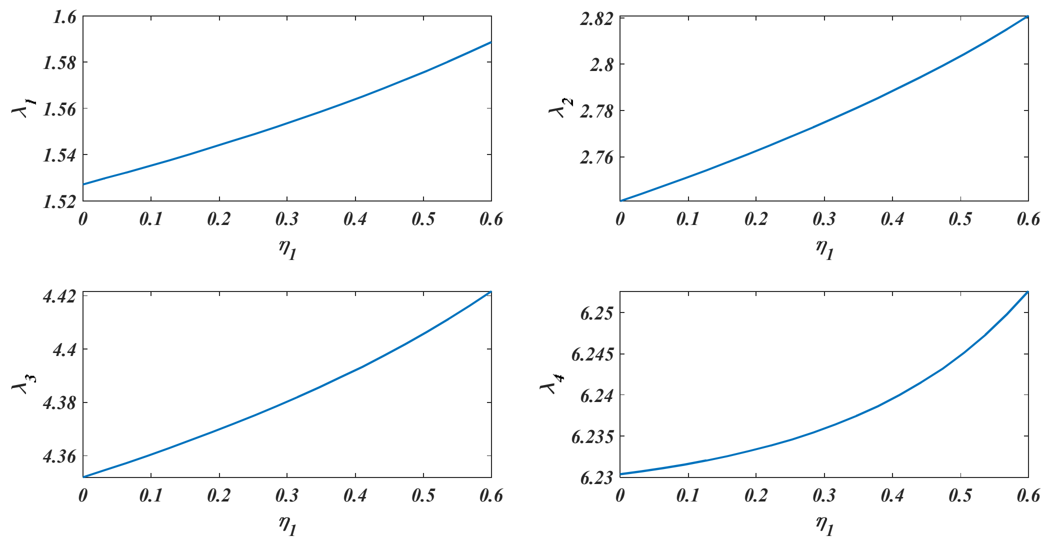

Fig. 12

Influence of the porosity coefficient on the natural frequencies of the sandwich microbeam.

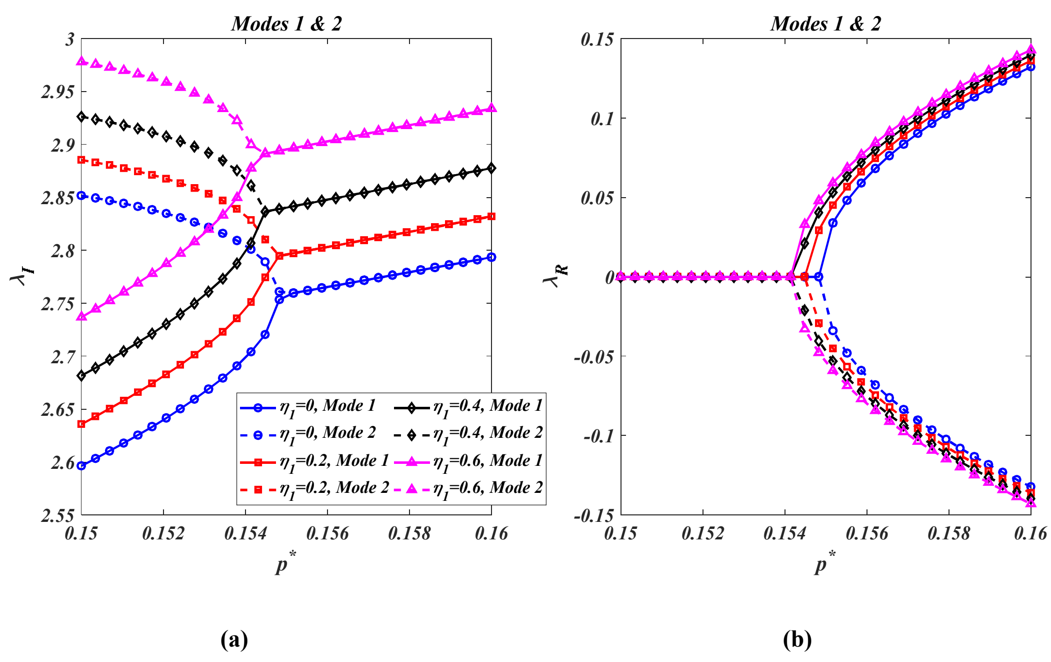

Fig. 13

Influence of the porosity coefficient on the aeroelastic stability of sandwich microbeam. (a) The imaginary part of frequency and (b) The real part of frequency.

Table 6, as well as Fig. 14, allows the evaluation of the impact of the pore distribution pattern on the natural frequencies and aeroelastic stability of the microbeam. Comparing the data in Table 6, it can be seen that SI distribution has the highest frequencies. At the same time, as shown in Fig. 14, this pattern achieves the best performance in terms of aeroelastic stability. This can be explained by examining Fig. 2, which exhibits that SI distribution implies larger pores closer to the beam's mid-surface. Thus, there is the least reduction in the bending stiffness of the beam. Table 6, as well as Fig. 14, demonstrate that the pore distribution pattern has a minimal effect on the natural frequencies and aeroelastic stability of the microbeam, similar to the porosity coefficient. Indeed, the critical aerodynamic pressure in the best case is less than one percent above the value in the worst option. This is because the porous core is less significant in determining the microbeam's stiffness compared to the nanocomposite facings.

Table 6
Influence of pore distribution patterns on the natural frequencies of the sandwich microbeam

	λ_1	λ_2	λ_3	λ_4
UD	1.5486	2.7676	4.3737	6.2344
SI	1.5488	2.7686	4.3749	6.2345
SII	1.5481	2.7665	4.3742	6.2401

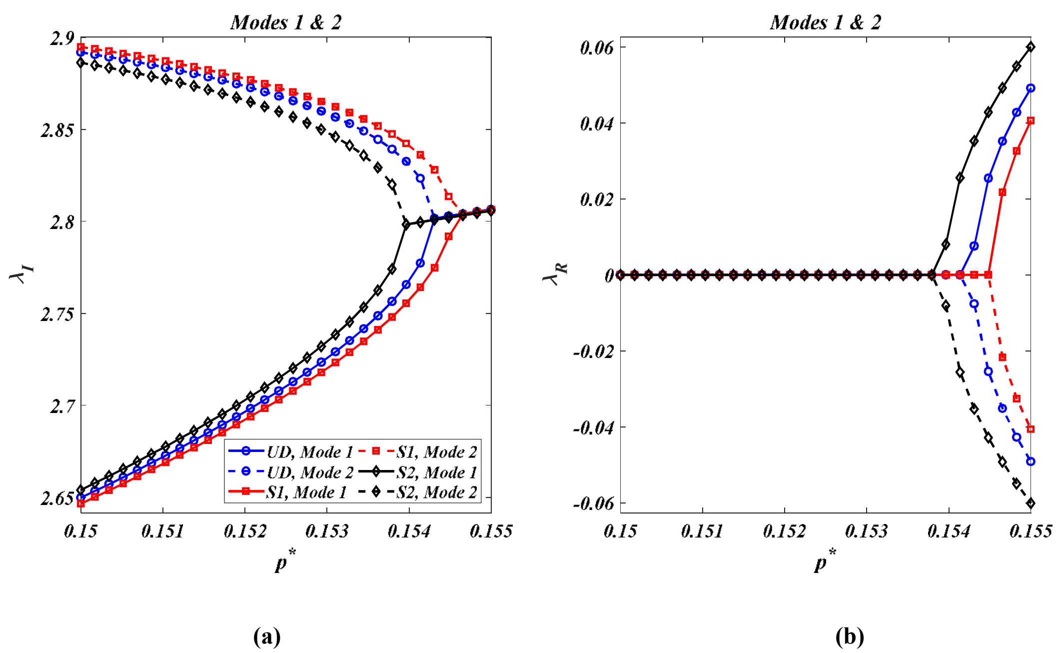

Fig. 14

Influence of pore distribution patterns on the aeroelastic stability of the sandwich microbeam. (a) The imaginary part of frequency and (b) The real part of frequency.

The influence of the CNTs mass fraction on both the natural frequencies and the aeroelastic stability of the microbeam is shown in Fig.15 and Fig.16. It was shown above that CNTs have very high elastic constants and a slightly lower density compared to the polymer matrix. Therefore, increasing the carbon nanotube mass fraction slightly reduces the mass of the microbeam and significantly increases its stiffness. The latter leads to an increase in the natural frequencies of the microbeam and therefore, an improved aeroelastic stability, which is visible in Fig. 15 and Fig. 16 . From the data presented in Fig. 15, by increasing the CNT mass fraction from 0 to 1.5% it is possible to improve the critical aerodynamic pressure by about 11%, according to Fig. 6. One should note that the addition of very significant quantities of CNTs is neither effective nor cost-efficient due to their high cost and, at very high mass fractions, due to the increased occurrence of aggregation phenomena.

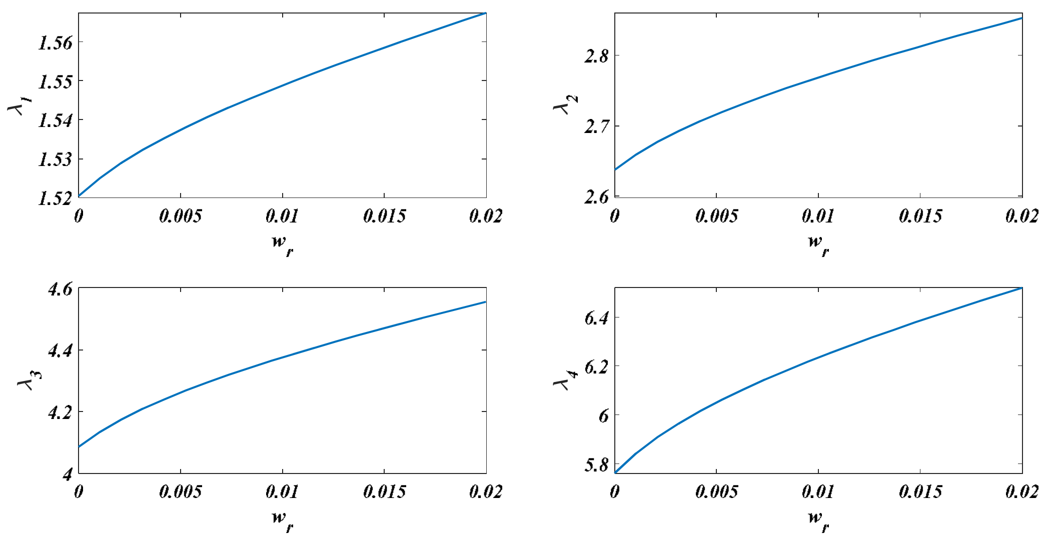

Fig. 15

Influence of carbon nanotube mass fraction on the natural frequencies of the sandwich microbeam.

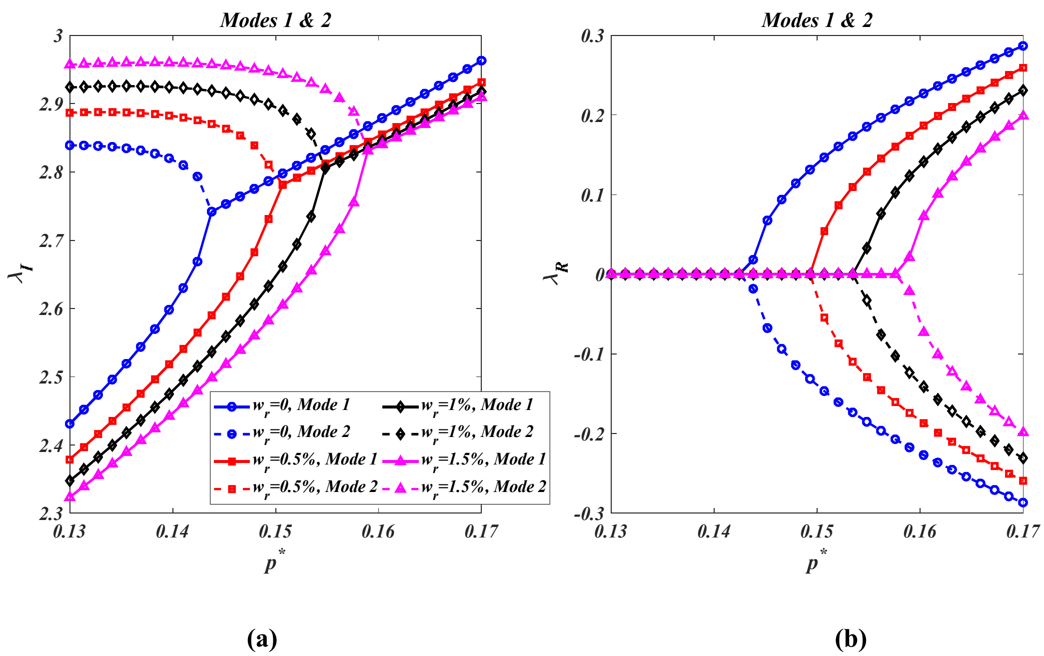

Fig. 16

Influence of carbon nanotube mass fraction on the aeroelastic stability of the sandwich microbeam. (a) The imaginary part of frequency and (b) The real part of frequency.

The study presented in Table 7 shows the effect of the type of CNTs on the natural frequencies of the microbeam, while Fig. 17 presents the effect on aeroelastic stability boundaries. Since CNTs with lower chiral indices have lower diameters, they also exhibit higher elastic constants, as indicated in Table 2. Thus, the use of CNTs with lower chiral indices as reinforcements is expected to increase the natural frequencies of the microbeam. Similarly, such beams are more stable due to reduced aeroelastic oscillations. As clearly shown in Table 6 and Fig. 17, this is the case. The effect of the CNTs types is profound such that the critical aerodynamic pressure of a microbeam under SWCNT beam 5,5 is 42% more than that under SWCNT beam 50, 50.

Table 7
Influence of the type of CNTs on the natural frequencies of the sandwich microbeam

	λ_1	λ_2	λ_3	λ_4
SWCNT (5,5)	1.5668	2.8483	4.5443	6.5034
SWCNT (10,10)	1.5488	2.7686	4.3749	6.2345
SWCNT (15,15)	1.5414	2.7355	4.3034	6.1196
SWCNT (20,20)	1.5372	2.7167	4.2623	6.0530
SWCNT (50,50)	1.5278	2.6739	4.1677	5.8986

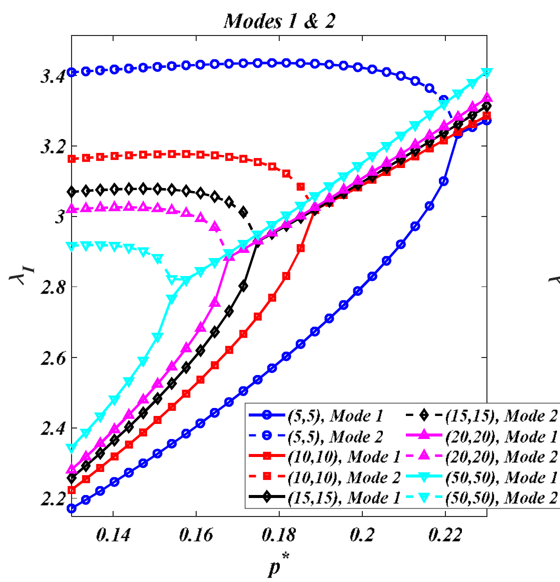

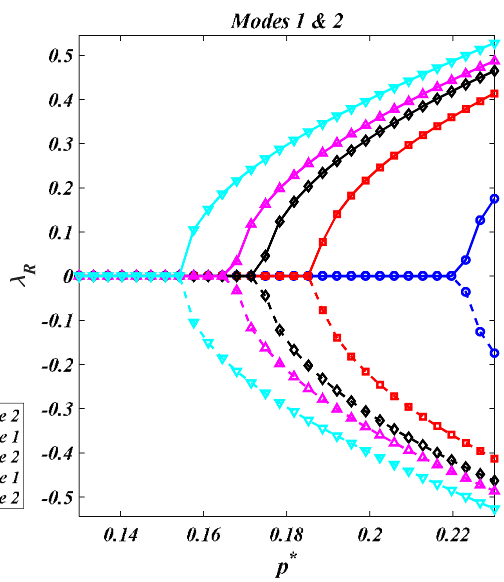

Fig. 17

Influence of the type of CNTs on the aeroelastic stability boundaries of the sandwich microbeam. (a) The imaginary part of frequency and (b) The real part of frequency.

Table 8 shows the impact of the CNT distribution pattern on the natural frequencies of the microbeam, and this fig. 18 shows it is influencing the aeroelastic stability boundaries. It can be seen that the only combination with the highest values of both natural frequencies and critical aerodynamic pressure is AV. In contrast, the lowest values belong to the VA combination. From this point, it can be inferred that to maximize the natural frequencies of the microbeam and attain the greatest benefit from an improvement in aeroelastic stability, CNTs should be distributed as close as possible to the microbeam's top and bottom surfaces. The explanation for this statement is that this distribution pattern causes the maximum rise in the bending stiffness of the microbeam. However, the impact of the CNTs distribution pattern is not very great, as even in the best scenario of AV, it is only 3% better than in the worst of VA. the maximum rise in the bending stiffness of the microbeam. However, the impact of the CNT distribution pattern is not very great, as even in the best scenario of AV, it is only 3% better than in the worst of VA .

Table 8
Influence of the carbon nanotube distribution pattern on the natural frequencies of the sandwich microbeam

	λ_1	λ_2	λ_3	λ_4
UU	1.5461	2.7575	4.3533	6.2038
AV	1.5488	2.7686	4.3749	6.2345
VA	1.5409	2.7344	4.3046	6.1274
AA or VV	1.5449	2.7519	4.3410	6.1836

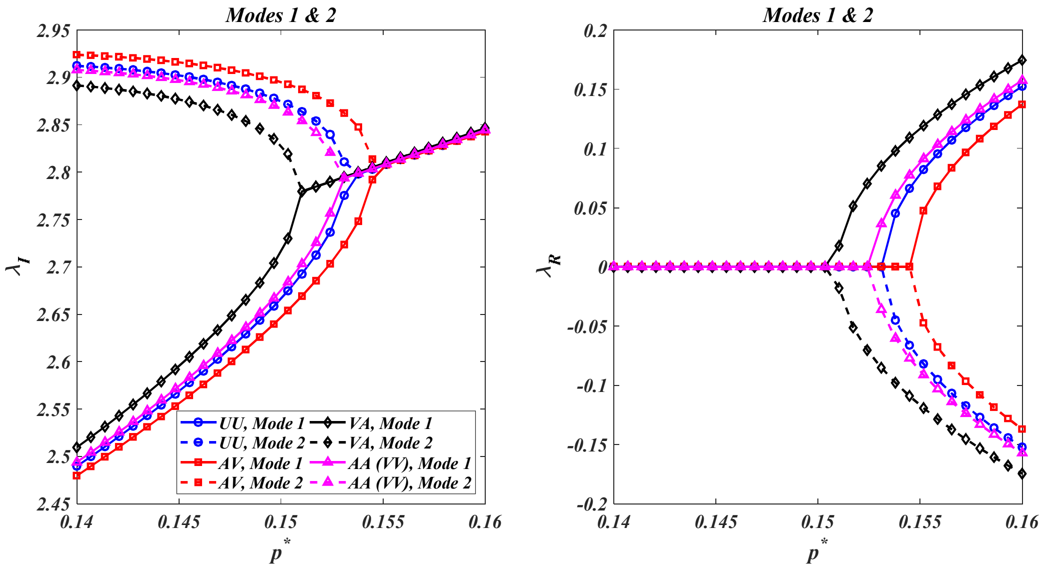

(a) (b)

Fig. 18

Influence of the carbon nanotube distribution pattern on the aeroelastic stability of the sandwich microbeam. (a) The imaginary part of frequency and (b) The real part of frequency.

Fig. 19 and Fig. 20 show the influence of the agglomeration coefficient η on the natural frequencies and the aeroelastic stability of the microbeam. According to Eq. 17,the increase of the agglomeration coefficient η means that a higher percentage of CNTs have accumulated.Since the agglomeration leads to a decrease in the elastic constants of the nanocompsite,as shown in fig. 19 and fig. 20,by increasing the agglomerationcoefficient η ,the natural frequencies decrease in all vibration modes and the aeroelastic stability of the microbeam decreases.Fig.20 shows that by increasing the agglomeration factor η from 0.2 to 0.8 , the critical aerodynamic pressure decreases by about 5%.

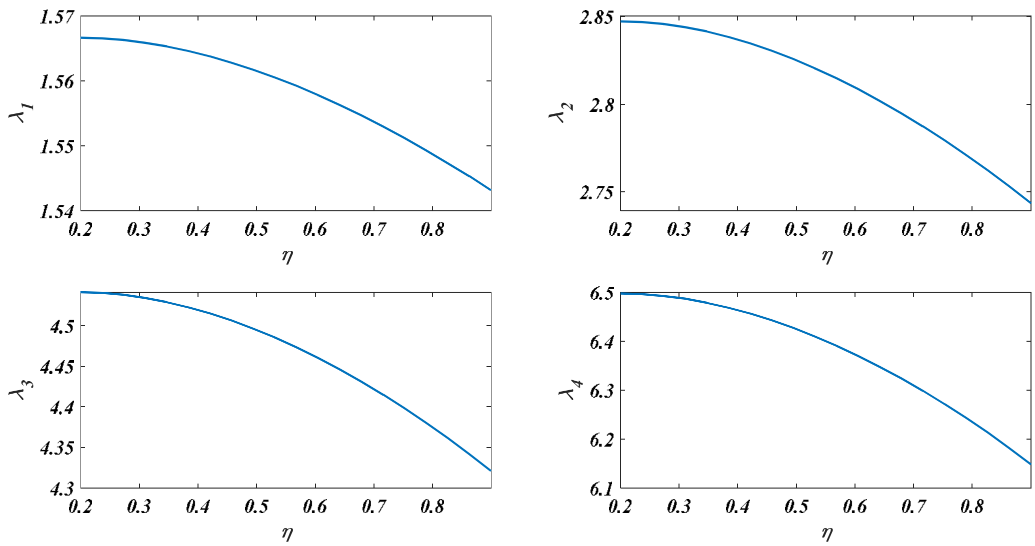

Fig. 19

Influence of the agglomeration coefficient η on the natural frequencies of the sandwich microbeam.

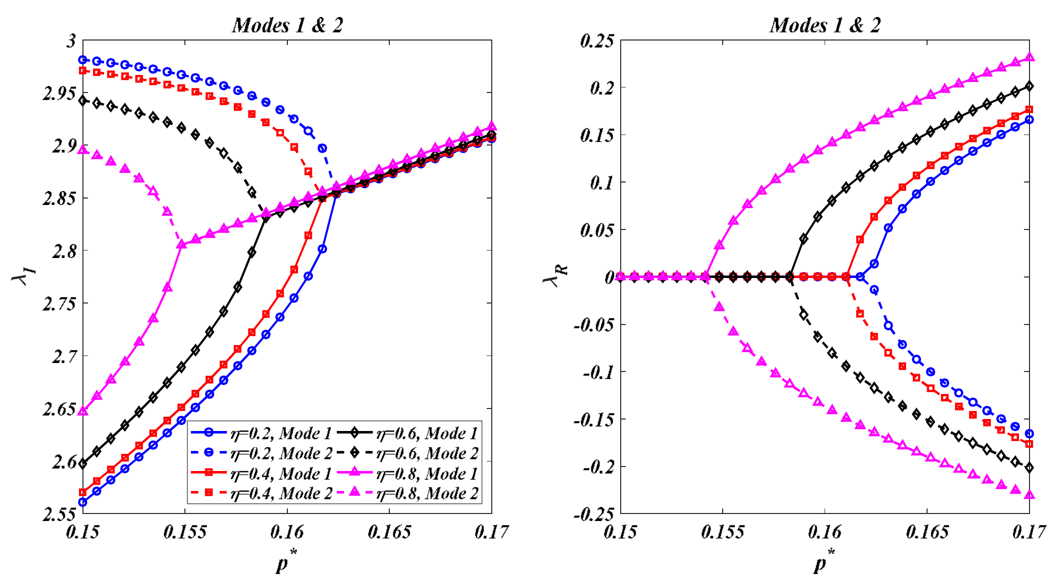

(a) **(b)**

Fig. 20

Influence of the agglomeration coefficient η on the aeroelastic stability of the sandwich microbeam. (a) The imaginary part of frequency and (b) The real part of frequency.

Fig. 21 and Fig. 22 display the impact of the elastic coefficient of the substrate on the natural frequencies and the aeroelastic stability of the microbeam. From Eq. 32, a decrease in k_w implies a commensurate reduction in the potential energy of the substrate, hence a lowering of high potential energy that enables high natural frequencies of all the vibrational modes. Consequently, on the expectation, the aeroelastic stability should be lowered by reducing implied potential energy exposure. However, Fig. 22 asserts a contrary state of affairs. Fig. 21 shows that when the k_w rises, there is a commensurate rise in potential energy, which generates high natural frequencies with higher aeroelastic stability. However, Fig. 22 reveals that in the second mode of Fig. 22, with increasing k_w, the two natural frequencies high natural frequencies. High increase and eventually become equal at a lower aerodynamic pressure, thus triggering the flutter behavior at the first mode. Fig. 22 demonstrates that with an increase in the k_w value from 0.1 to 0.4, the critical aerodynamic pressure declines by just over 1%.

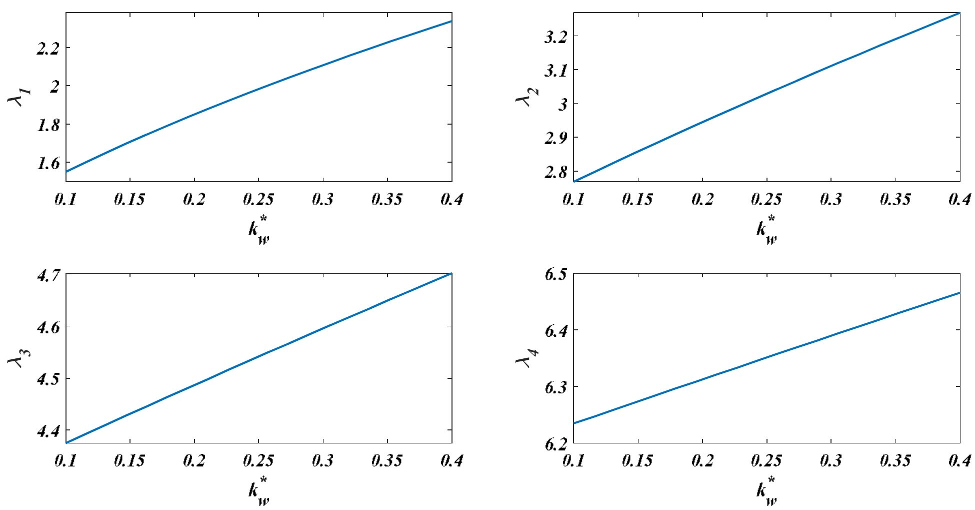

Fig. 21

Influence of the elastic coefficient of the substrate on the natural frequencies of the sandwich microbeam.

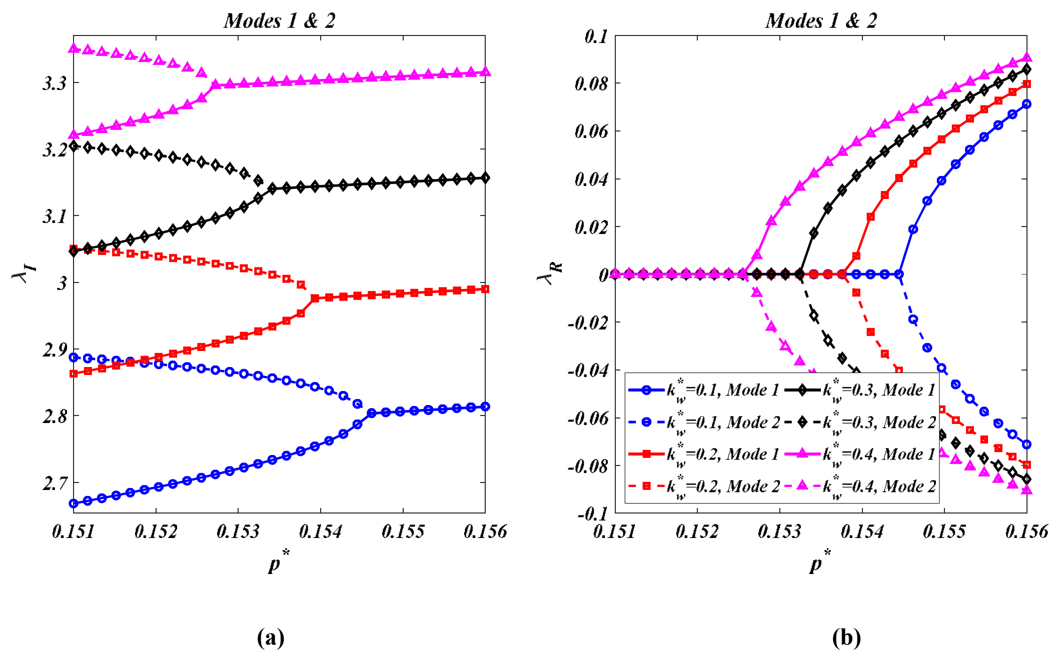

Fig. 22

Influence of the elastic coefficient of the substrate on the aeroelastic stabiity of the sandwich microbeam. (a) The imaginary part of frequency and (b) The real part of frequency.

The effects of the foundation shear coefficient on the natural frequencies and flutter instability boundaries of the microbeam are investigated in Fig. 23and 24. As can be seen from Eq. 32, increasing the foundation shear coefficient increases the foundation potential energy, which, as shown in Fig. 24, results in an increase in the natural frequencies of the microbeam in all vibration modes, similar to what was observed for the effect of the foundation elastic coefficient. Fig.24 shows that, in contrast to what was observed for the foundation elastic coefficient, increasing the foundation shear coefficient not only increases the values of the natural frequencies in the first and second vibration modes but also increases the difference between them, which results in an increase in the critical aerodynamic pressure value and an improvement in the flutter instability of the microbeam. As can be seen from Fig.24, with an increase in the foundation shear coefficient in the dimensionless form from 0 to 0.015, the critical aerodynamic pressure increases by about 400%, which shows the significant effect of this foundation coefficient.

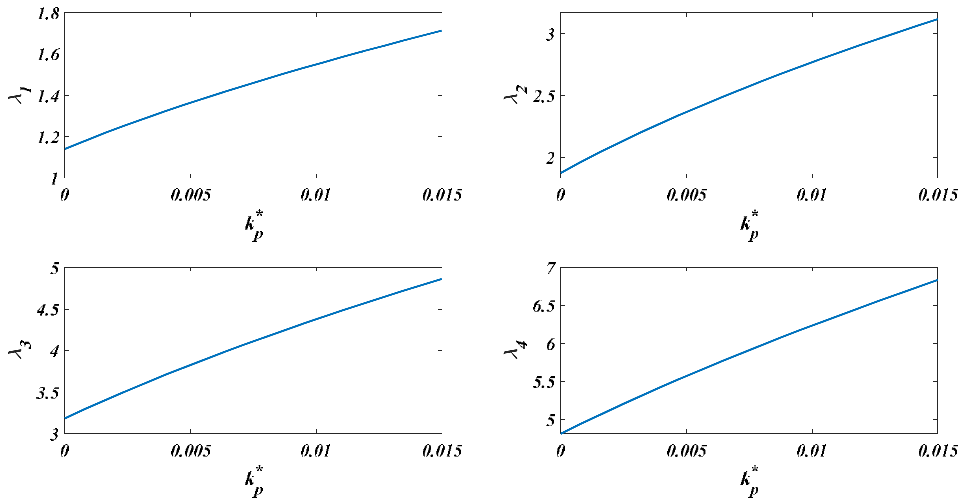

Fig. 23

Influence of the shear coefficient of the substrate on the natural frequencies of the sandwich microbeam.

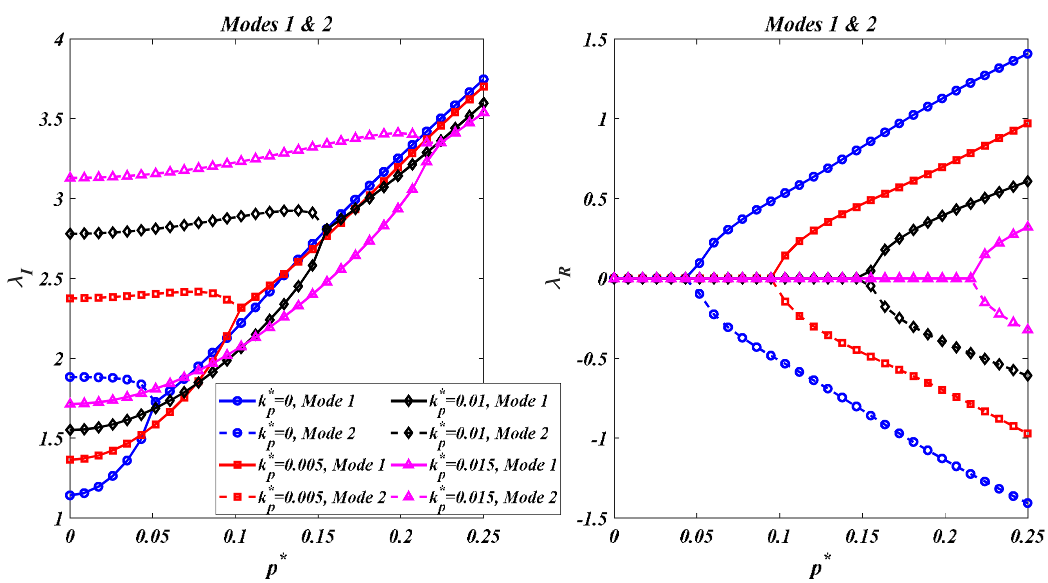

(a) (b)

Fig. 24

Influence of the shear coefficient of the substrate on the aeroelastic stability of the sandwich microbeam. (a) The imaginary part of frequency and (b) The real part of frequency.

8 CONCLUSION

In this paper, the free vibration and flutter analyses of sandwich microbeams with FG porous core and FG accumulated CNTs face sheets under supersonic fluid flow. The sandwich microbeam was modeled according to different theories, such as the EBT, TBT, and RBT; also, the side effects were taken into account by coupling the MCST with beam theories. The piston theory was used to estimate the aerodynamic pressure because of the fluid flow, and the Pasternak foundation was considered to model the elastic foundation. Moreover, Hamilton's principle was used to derive the governing equations and boundary conditions. For the approximate solution of the governing equations under various boundary conditions, the DQM was used. Also, the accurate solution for microbeam was proposed by solving the boundary value problem using the Navier method.
In summation, the key results from this study can be generalized as:

- The aeroelastic stability of the microbeam increases as the level of constraint on the boundaries of the microbeam increases thus the highest critical aerodynamic pressure will be present in a clamped-clamped microbeam while the smallest in a clamped-free microbeam.
- As the core porosity ratio increases, the natural frequencies of the microbeam increase, but the aeroelastic stability decreases.
- To achieve the highest natural frequencies and improve aeroelastic stability, the distribution of holes in the microbeam core should be such that the larger holes are located as close as possible to the mid-surface of the microbeam.
- To maximize the increase in natural frequencies and achieve the maximum improvement in the aeroelastic stability of the microbeam, CNTs distributed as close as possible to the top and bottom sheets of the microbeam.
- By increasing the elastic and shear coefficients of the foundation, the natural frequencies of the microbeam increase in all vibration modes.As the shear modulus of the foundation increases, the aeroelastic stability of the microbeam improves. However, increasing the elastic modulus of the substrate leads to a decrease in the aeroelastic stability of the microbeam.

REFERENCES

1. Subbaratnam B., 2024, Dynamic Stability of Beam on Elastic Foundation Including Higher Transition Foundation, IntechOpen. doi: 10.5772/intechopen.113009.
2. Magnucki., Krzysztof., Ewa Magnucka-Blandzi.,2024, Dynamic Stability of a Three-Layer Beam– Generalisation of the Sandwich Structure Theory, *acta mechanica ,* doi 102478/ama-2024-0001.
3. Sourani P., Ghorbanpour Arani A., Hashemian M., Niknejad S.,2024, Nonlinear dynamic stability analysis of CNTs reinforced piezoelectric viscoelastic composite nano/micro plate under multiple physical fields resting on smart foundation, *Mechanical Engineers,* doi:10.1177/09544062231196078.
4. Addou F. Y., Bourada F., Tounsi A., Bousahla A. A., Tounsi A., Benrahou K. H., Albalawi H., 2024, Effect of porosity distribution on flexural and free vibrational behaviors of laminated composite shell using, *Archiv.Civ.Mech.Eng* ,https://doi.org/10.1007/s43452-024-00894-w.
5. Van N. T. H., van Minh P., Duc N. D., 2024,Finite-element modeling for static bending and free vibration analyses of double-layer non-uniform thickness FG plates taking into account sliding interactions, *Archives of Civil and Mechanical Engineering* , https://doi.org/10.1007/s43452-024-00914-9.
6. Mohanty M., Maity R., Pradhan M., Dash P., 2023, Parametric stability of Timoshenko taper sandwich beam on Pasternak foundation, Materials Today, https://doi.org/10.1016/j.matpr.2023.03.735.
7. Civalek Ö., Ersoy H., Uzun B.,Ersoy H., Yayli M. Ö., 2023, Dynamics of a FG porous microbeam with metal foam under deformable boundaries, *Acta Mech*, https://doi.org/10.1007/s00707-023-03663-7.
8. Ghorbanpour-Arani A., Khoddami Maraghi Z., Ghorbanpour Arani A., 2023, The Frequency Response of Intelligent Composite Sandwich Plate Under Biaxial In-Plane Forces. Journal of Solid Mechanics, https://doi.org/10.22034/jsm.2020.1895607.1563.
9. Gia Phi B., Van Hieu D., Sedighi H.M., *Sofiyev A.H.,* 2022, Size-dependent nonlinear vibration of functionally graded composite micro-beams reinforced by carbon nanotubes with piezoelectric layers in thermal environments, *Acta Mech*,https://doi.org/10.1007/s00707-022-03224-4.
10. Wu X.W., Zhu L.F., Wu Z.M., Ke L.L., 2022, Vibrational power flow analysis of Timoshenko microbeams with a crack, *Composite Structures*, http://.org/10.1016/j.compstruct.2022.115483.

11. Wang Y.Q., Zhao H.L., Ye C., Zu J.W., 2022, A porous microbeam model for bending and vibration analysis based on the sinusoidal beam theory and modified strain gradient theory. *International Journal of Applied Mechanics*,https://doi.org/10.1142/S175882511850059.
12. Karamanli A., Vo T.P., 2021, Bending, vibration, buckling analysis of bi-directional FG porous microbeams with a variable material length scale parameter, *Applied Mathematical Modelling*, http://doi.org/10.1016/j.apm.2020.09.058.
13. Arshid E., Amir S., 2021, Size-dependent vibration analysis of fluid-infiltrated porous curved microbeams integrated with reinforced functionally graded graphene platelets face sheets considering thickness stretching effect, *Proceedings of the Institution of Mechanical Engineers, Part L: Journal of Materials: Design and Applications*, https://doi.org/10.1177/1464420720985556.
14. Tlidji Y., Benferhat R., Tahar H.D., 2021, Study and analysis of the free vibration for FGM microbeam containing various distribution shape of porosity, *Structural Engineering and Mechanics, An Int'l Journal*, https://doi.org/10.12989/sem.2021.77.2.217.
15. Haghparast E., Ghorbanpour-Arani A ., Ghorbanpour Arani A ., 2020, Effect of Fluid–Structure Interaction on Vibration of Moving Sandwich Plate with Balsa Wood Core and Nanocomposite Face Sheets, International Journal of Applied Mechanics, https://doi.org/10.1142/S1758825120500787.
16. Enayat S., Hashemian M., Toghraie D., Jaberzadeh E., 2020,A comprehensive study for mechanical behavior of functionally graded porous nanobeams resting on elastic foundation, *Journal of the Brazilian Society of Mechanical Sciences and Engineering*, https://doi.org/10.1007/s40430-020-02474-4.
17. Ghorbanpour Arani A., Soleymani T., 2019, Size-dependent vibration analysis of a rotating MR sandwich beam with varying cross section in supersonic airflow. *International Journal of Mechanical Sciences*, https://doi.org/10.1016/j.ijmecsci.2018.11.024.
18. Amir S., Soleimani Javid Z., Arshid E., 2019, Size□dependent free vibration of sandwich micro beam with porous core subjected to thermal load based on SSDBT, *ZAMM□Journal of Applied Mathematics and Mechanics/Zeitschrift für Angewandte Mathematik und Mechanik*,https://doi.org/10.1002/zamm.201800334.
19. Wang Y.Q., Zhao H.L., Ye C., Zu J.W., 2018,A porous microbeam model for bending and vibration analysis based on the sinusoidal beam theory and modified strain gradient theory, *International Journal of Applied Mechanics* , https://doi.org/10.1142/S175882511850059.
20. Subbaratnam B, 2024, Dynamic Stability of Beam on Elastic Foundation Including Higher Transition Foundation, IntechOpen. doi: 10.5772/intechopen.113009.
21. Magnucki, Krzysztof, Ewa Magnucka-Blandzi,2024, Dynamic Stability of a Three-Layer Beam– Generalisation of the Sandwich Structure Theory, *acta mechanica ,* doi 102478/ama-2024-0001.
22. Adab N., Arefi M., 2023,Vibrational behavior of truncated conical porous GPL-reinforced sandwich micro/nano-shells, *Engineering with Computers*. https://doi.org/10.1007/s00366-021-01580-8.
23. Chen D., Kitipornchai S., Yang J., 2016, Nonlinear free vibration of shear deformable sandwich beam with a functionally graded porous core, *Thin-Walled Structures* , https://doi.org/10.1016/j.tws.2016.05.025.
24. Reddy J.N., 2017,*Energy principles and variational methods in applied mechanics*, John Wiley & Sons, Hoboken, New Jersey, United States.
25. Khoddami Maragh Z., Amir S., Arshid E., 2024,On the natural frequencies of smart circular plates with magnetorheological fluid core embedded between magneto strictive patches on Kerr elastic substance, Mechanics Based Design of Structures and Machines , https://doi.org/10.1080/15397734.2022.2156885.
26. Şimşek M., Reddy J.N., 2013, Bending and vibration of functionally graded microbeams using a new higher order beam theory and the modified couple stress theory. *International Journal of Engineering Science* , https://doi.org/10.1016/j.ijengsci.2012.12.002.
27. Tornabene F., Bacciocchi M., Fantuzzi N., Reddy J.N., 2019,Multiscale approach for three□phase CNT/polymer/fiber laminated nanocomposite structures, *Polymer composites*,https://doi.org/10.1002/pc.24520.
28. Sadd M.H., 2009, *Elasticity theory, applications, and numerics*, Elsevier, Cambridge, Massachusetts, United States.
29. Rajesh K., Saheb K.M., 2017, Free vibrations of uniform timoshenko beams on pasternak foundation using coupled displacement field method, *Archive of Mechanical Engineering*, https://doi.org/ 10.1515/meceng-2017-0022.
30. Soltan Arani A.H., Ghorbanpour Arani A., Khoddami Maraghi Z., 2024,Nonlocal quasi-3d vibration/analysis of three-layer nanoplate surrounded by Orthotropic Visco-Pasternak foundation by considering surface effects and neutral surface concept, Mechanics Based Design of Structures and Machines , http://doi.org/10.1080/15397734.2024.2348103.
31. Ashley H., Zartarian G., 1956, Piston theory-a new aerodynamic tool for the aeroelasticity, *Journal of the aeronautical sciences* , https://doi.org/10.2514/8.3740.
32. Ghorbanpour Arani A., Kiani F., 2019, Afshari H.: Aeroelastic Analysis of Laminated FG-Cntrc Cylindrical Panels Under Yawed Supersonic Flow, *International Journal of Applied Mechanics* , https://doi.org/10.1142/S1758825119500522.
33. Hosseini M., Ghorbanpour Arani A., Karamizadeh M.R., Afshari H., Niknejad S., 2019, Aeroelastic analysis of cantilever non-symmetric FG sandwich plates under yawed supersonic flow, *Wind and Structures*, https://doi.org/10.12989/was.2019.29.6.457.
34. Bellman R., Casti J., 1971, Differential quadrature and long-term integration, *Journal of mathematical analysis and Applications*, https://doi.org/10.1016/0022-247X(71)90110-7.

35. Bellman R., Kashef B., Casti J., 1972, Differential quadrature: a technique for the rapid solution of nonlinear partial differential equations. *Journal of computational physics*, *https://api.semanticscholar.org/CorpusID:122053474.*
36. Bert C.W., Malik M., 1956, Differential quadrature method in computational mechanics: a review, *Applied Mechanics Reviews*,DOI:10.1115/1.3101882.
37. Jahangiri S., Ghorbanpour Arani A., Khoddami Maraghi Z., 2024,Dynamics of a rotating ring-stiffened sandwich conical shell with an auxetic honeycomb core, Applied Mathematics and Mechanics , https://doi.org/10.1007/s10483-024-3124-7.
38. Khoddami Maraghi Z., 2019, Flutter and divergence instability of nanocomposite sandwich plate with magneto strictive face sheets, Journal of Sound and Vibration ,http://doi.org/10.1016/j.jsv.2019.06.002.
39. Chen D., Yang J., Kitipornchai S., 2016, Free and forced vibrations of shear deformable functionally graded porous beams, *International journal of mechanical sciences*,